

THESIS FOR THE DEGREE OF LICENTIATE OF ENGINEERING

Atom probe tomography of Zircaloy-2 exposed to  
boiling water reactor operation

JOHAN ERIKSSON

Department of Physics

CHALMERS UNIVERSITY OF TECHNOLOGY

Gothenburg, Sweden 2021

Atom probe tomography of Zircaloy-2 exposed to boiling water reactor operation  
JOHAN ERIKSSON

© JOHAN ERIKSSON, 2021.

Department of Physics  
Chalmers University of Technology  
SE-412 96 Gothenburg  
Sweden  
Telephone + 46 (0)31-772 1000

Cover:

Atom probe tomography reconstruction of a disc-shaped Fe–Ni cluster and a spheroidal Fe–Cr cluster in Zircaloy-2 exposed to nine annual cycles of boiling water reactor operation.

Chalmers Reproservice  
Gothenburg, Sweden 2021

## Abstract

Zirconium alloys are used as cladding tubes for the fuel in nuclear reactors. In boiling water reactors (BWRs), the alloy Zircaloy-2, which contains the alloying elements Sn, Fe, Cr, Ni, and O, is commonly used. In this thesis, results from atom probe tomography studies of Zircaloy-2 exposed to three and nine annual cycles of BWR operation are presented. The alloying elements were observed to be redistributed after reactor exposure. Clusters of Fe and Cr or Fe and Ni were observed at expected positions of radiation-induced  $\langle a \rangle$  type dislocation loops. Regions containing mainly Fe–Cr clusters were much more common than regions containing mainly Fe–Ni clusters. The Fe–Cr clusters appeared dense and spheroidal, whereas the Fe–Ni clusters appeared dilute and disc-shaped. The Fe–Ni discs occupied planes that correspond to all three families of first-order prismatic planes but with deviation from perfect  $\langle c \rangle$  axis alignment. Many grain boundaries were observed, and there were large grain-to-grain variations in cluster number density and cluster composition. Regarding cluster number density, there was on average no difference between three cycles and nine cycles. After nine cycles the clusters were on average larger and contained more Cr. Sn was observed to cluster in regions where there were no Fe–Cr or Fe–Ni clusters. Enrichment of Sn and Fe and small amounts of Cr and Ni was observed at grain boundaries. After nine cycles, but not after three cycles, enrichment of Sn, Fe, and Ni at ring-shaped features interpreted to be radiation-induced  $\langle c \rangle$  component loops was observed. Hydrogen was observed to be preferentially located outside a partially dissolved  $\text{Zr}(\text{Fe},\text{Cr})_2$  second phase particle that also contained Ni and Si. The present work demonstrates that the well-known dislocation loops have a chemistry, in the form of clusters of different types and shapes, that might substantially affect mechanisms degrading the cladding tubes, e.g. irradiation growth, corrosion, and hydrogen pickup.

**Keywords:** Zirconium alloys, Zircaloy-2, Radiation effects, Dislocation loops, Clustering, Nuclear fuel claddings, Boiling water reactor, Atom probe tomography



## Preface

The research work presented in this thesis was carried out at the Division of Microstructure Physics at the Department of Physics, Chalmers University of Technology, Gothenburg, Sweden, during the time period March 2018–April 2021, under the supervision of Associate Professor Mattias Thuvander, Professor Hans-Olof Andrén, and Doctor Mohammad Sattari. The work was performed as part of the international MUZIC-3 consortium and was funded by Westinghouse Electric Sweden AB, Vattenfall AB, OKG AB, and the Electric Power Research Institute (EPRI).

### List of appended papers

- I. *An atom probe tomography study of the chemistry of radiation-induced dislocation loops in Zircaloy-2 exposed to boiling water reactor operation*  
J. Eriksson, G. Sundell, P. Tejlund, H.-O. Andrén, M. Thuvander  
Journal of Nuclear Materials 550, 152923 (2021).
- II. *Nanoscale chemistry of Zircaloy-2 exposed to three and nine annual cycles of boiling water reactor operation — an atom probe tomography study*  
J. Eriksson, G. Sundell, P. Tejlund, H.-O. Andrén, M. Thuvander  
In manuscript.

For both the appended papers, I analysed and evaluated the experimental data and wrote the paper, with input from co-authors.



## Table of contents

<b>1. Introduction</b> .....	<b>1</b>
1.1 Background .....	1
1.2 Aim .....	1
<b>2. Nuclear reactors</b> .....	<b>3</b>
<b>3. Zr alloy nuclear fuel claddings</b> .....	<b>7</b>
3.1 Types of alloys .....	7
3.2 Crystallography .....	8
3.3 Chemistry .....	11
3.4 Manufacture and texture .....	12
<b>4. Irradiation effects on Zr alloys</b> .....	<b>13</b>
4.1 Point defects and dislocation loops .....	13
4.2 Irradiation growth and irradiation creep .....	16
4.3 SPP dissolution and alloying element redistribution .....	17
4.4 Pellet–cladding interaction.....	18
<b>5. Corrosion of Zr alloys</b> .....	<b>19</b>
5.1 General corrosion phenomena in autoclave and in reactor .....	19
5.2 Effects of SPPs, alloying elements, and impurities .....	22
<b>6. H pickup and hydride phases in Zr alloys</b> .....	<b>23</b>
<b>7. Experimental techniques</b> .....	<b>27</b>
7.1 Atom probe tomography .....	27
7.1.1 Overview .....	27
7.1.2 Specimen reconstruction and data evaluation .....	29
7.1.3 Limitations and artefacts .....	32
7.1.4 Atom probe tomography of Zr alloys .....	33
7.2 Sample preparation .....	35
7.2.1 Electropolishing .....	35
7.2.2 Focused ion beam–scanning electron microscopy .....	36
<b>8. Material studied</b> .....	<b>39</b>
<b>9. Summary of results and discussion</b> .....	<b>41</b>
9.1 Summary of Paper I .....	41
9.2 Summary of Paper II .....	43
9.3 Discussion .....	44
<b>10. Future work</b> .....	<b>47</b>
<b>Acknowledgements</b> .....	<b>49</b>
<b>References</b> .....	<b>51</b>



# 1. Introduction

The applications of the material in focus of this thesis are within the nuclear industry. In this chapter, the reason for performing the research of this thesis and the aim of the study presented in the thesis are explained.

## 1.1 Background

Nuclear power is one of the major methods of producing electricity in the world. In 2020, 10% of world electricity production was generated by nuclear power [1]. In studies comparing the main sources of electricity production, nuclear power is, per unit electric energy generated, among the sources with lowest greenhouse gas emissions [2], lowest land use [3], and lowest impact on human health [4]. If an increased demand for electricity by a growing human population is to be met with low greenhouse gas emissions and reasonably low impacts on biodiversity and human health, nuclear power thus has the capability of making a significant contribution. A more efficient use of the nuclear fuel would allow for more electricity to be generated from the existing uranium reserves and would lead to a lower amount of highly radioactive waste being produced in nuclear reactors. In the vast majority of current reactor designs, the performance of zirconium alloys is one of the factors limiting more efficient fuel utilisation, thereby motivating research aiming at improving the properties of Zr alloys. Improved Zr alloys that are more resistant to degrading mechanisms might, furthermore, enable safer operation of nuclear power plants.

According to the International Atomic Energy Agency (IAEA), in the beginning of 2021, worldwide, there were 443 operating nuclear power reactors and 50 under construction [1]. In almost all of these nuclear reactors, Zr alloys are used as structural core components or cladding tubes for the nuclear fuel.

In the harsh environment inside the core of a nuclear reactor in operation, a combination of radiation effects, corrosion, and hydrogen pickup (HPU) contributes to degradation of the cladding. Although a lot of research to understand these degrading mechanisms and their interrelation has been undertaken during the approximately 70 years that Zr alloys have been in use in nuclear reactors, their detailed nature still is unclear.

## 1.2 Aim

Radiation-induced defects in Zr alloys lead to dimensional changes of the material while the volume remains constant, a phenomenon termed irradiation growth [5]. The alloying elements affect irradiation growth [5], corrosion [6], and HPU [7]. It is thus of interest to study the relation between radiation-induced defects and alloying elements.

The aim of this study is to investigate the nanoscale and microscale chemistry of Zr alloys exposed to nuclear reactor operation and to study how the chemistry at these length scales evolves over time, in order to get information that can be used to understand how the degradation of the Zr alloys is affected by alloying elements. Evaluation of data from previously performed atom probe tomography (APT) studies of Zr alloy fuel claddings exposed to reactor operation has been performed in this work.

The main objectives of this research are to investigate the chemistry of radiation-induced dislocation loops and to compare the nanoscale and microscale chemistry of the Zr alloy Zircaloy-2 exposed to different operating times, and hence different neutron fluences, in a commercial boiling water reactor (BWR). The exposure times of the two samples investigated in the two papers of this thesis were three years and nine years. Between these two levels of exposure there is a large difference in corrosion and HPU. The metal close to metal/oxide interface is the region that has been investigated, as the microstructural and chemical evolution in this region are believed to have a large impact on the corrosion and HPU of the material.

## 2. Nuclear reactors

This chapter describes the most common types of nuclear reactors and the role of Zr alloys in these reactors. Emphasis is on light water reactors (LWRs).

A variety of nuclear reactor designs exists, and there are multiple ways of classifying reactor types. Common ways are to classify according to the type of nuclear reaction occurring, according to the cooling medium, or according to the moderator material. Most nuclear reactors are thermal fission reactors, utilising thermal neutrons, i.e. neutrons of approximate energy 0.025 eV, to induce fission in the nuclear fuel [8]. Of the thermal reactors, LWRs constitute the most common subclass [9]. In LWRs, water is used for neutron moderation and cooling of the fuel. The name light water reactor is used to distinguish LWRs from heavy water reactors, which instead use heavy water for neutron moderation and cooling.

The nuclear fuel in LWRs consists of cylindrical UO<sub>2</sub> pellets, typically slightly less than 1 cm in diameter and a little larger in height [10]. These pellets are placed in cladding tubes made of Zr alloys, having a height of approximately 4 m, a diameter around 1 cm, and a wall thickness in the approximate range 0.6–0.8 mm [11]. The top and bottom of the tubes are sealed by welded end plugs, and He gas under pressure (ranging from 1–35 bar depending on design) is used to maintain a gap between the tube inside and the fuel pellets [10]. The stack of pellets is held in position by a spring or a clip from the topmost pellet to the top plug. The space between the stack of pellets and the top plug is called the plenum region and is the volume in which gases released in the fission process are contained (unless the integrity of the fuel rod is broken). A number of cladding tubes are grouped together to form a fuel assembly, and several hundreds of fuel assemblies are grouped together to form the core of the reactor. The core is located inside a reactor pressure vessel. The water used as cooling medium and moderator flows through the core. Thus, the Zr cladding tubes, which are in direct contact with the water, function as a barrier between the fuel and the water.

Compared with natural U, the U in the fuel pellets in LWRs is isotopically enriched in <sup>235</sup>U. The isotopic percentage of <sup>235</sup>U in fresh fuel is 3–5 %, the rest, except for trace amounts of <sup>234</sup>U, being <sup>238</sup>U. In a fast neutron flux, <sup>238</sup>U can, via neutron capture succeeded by β<sup>-</sup> decays, be transmuted to <sup>239</sup>Pu [12]. Thermal neutrons can induce fission of <sup>235</sup>U and <sup>239</sup>Pu [12]. In each fission event, one of these nuclides is split into two smaller nuclides, called fission fragments, and a few fast neutrons, on average approximately 2.4 for <sup>235</sup>U and 2.9 for <sup>239</sup>Pu [8]. The fast neutrons are moderated, i.e. slowed down, by the water in the reactor to reach thermal energies. When thermal, the neutrons can induce fission in other <sup>235</sup>U and <sup>239</sup>Pu nuclei. In a nuclear reactor, a critical chain reaction is sustained, i.e. the neutrons released in one fission event give on average rise to exactly one new fission event. The energy released is large, about 200 MeV per fission event, and is imparted as kinetic energy of the fission fragments. When the fission fragments slow down, the temperature inside the fuel pellet increases. Heat is conducted through the pellet and through the Zr alloy cladding (which is exposed to approximately 400 °C on the inside and about 300 °C on the outside) to increase the thermal energy of the coolant water. This thermal energy is converted to electricity via turbines and generators.

There are two types of LWRs, pressurised water reactors (PWRs) and BWRs. In PWRs there are two water circuits, the primary and the secondary. The water of the primary circuit is heated while passing through the core in the reactor pressure vessel, is cooled in steam generators, and is pumped back into the reactor pressure vessel. At all times, the pressure of

the primary circuit is kept high enough to keep its water liquid. The water of the secondary circuit is transformed to steam in the steam generators, passes through the turbines, is condensed in the condensers, and is pumped back into the steam generators. In BWRs, the water that passes through the core is heated and starts boiling inside the reactor pressure vessel. The steam thus generated goes to the turbines, is condensed in the condensers, and is pumped back into to the reactor pressure vessel. The typical operating pressure in a PWR core is around 15 MPa, and the temperature of the outgoing water from the core is around 320 °C [13]. The pressure of a BWR core is around 7 MPa, and the temperature of the steam is usually 286 °C [13]. A schematic of a PWR and a BWR is shown in Figure 2.1.

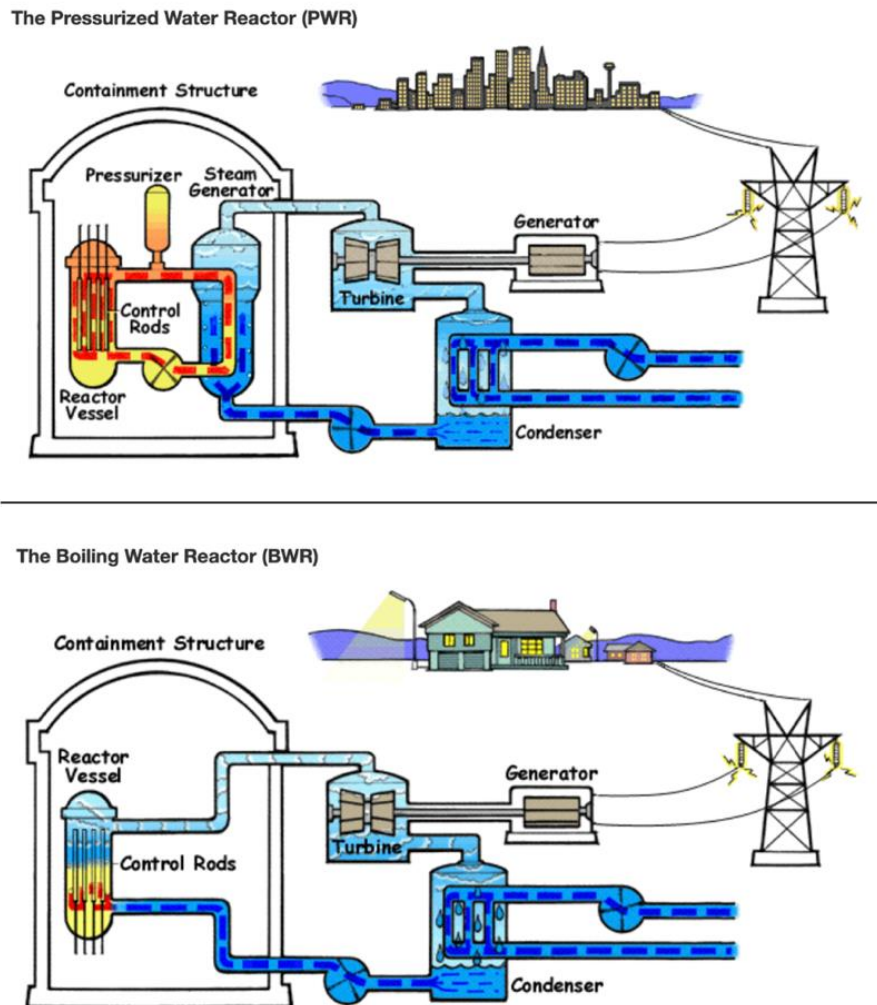


Figure 2.1: Schematic of a PWR and a BWR. From [14] and [15].

The design of the core differs between PWRs and BWRs. In both types of reactors, the fuel assemblies are arrays of fuel rods held together with so-called fuel rod spacer grids to keep the rods in correct position. The PWR fuel assemblies are generally quadratic with  $14 \times 14$  to  $18 \times 18$  rods in each array for non-Russian reactor designs and hexagonal with up to more than 300 fuel rods in each array for Russian reactor designs, so-called VVERs (or WWERs). Control rods containing neutron absorbing material that stops the nuclear chain reaction can be inserted at positions in the fuel assemblies where the fuel rods have been replaced by control rod guide tubes. The number of fuel rods in PWR assemblies is inherent to the reactor design and cannot be changed. In BWR fuel assemblies, the arrays are quadratic with, most

commonly,  $10 \times 10$  or  $11 \times 11$  rods in each array. For reasons of flow stability, each fuel assembly is surrounded by a channel box made of Zr alloy. Fuel assemblies are grouped together in units of four, and, in each group, control blades containing neutron-absorbing material can be inserted between the channel boxes. The number of fuel rods in BWR assemblies is not inherent to the reactor design and varies between different assembly designs. A larger number of fuel rods in the assembly gives a higher power density, and modern fuel assemblies therefore have a higher number of fuel rods than older designs. The total number of fuel rods is in the approximate range 40 000–60 000 in a PWR core and 60 000–90 000 in a BWR core [10]. Fuel assemblies for BWRs and PWRs (of non-Russian design) are shown in Figure 2.2.

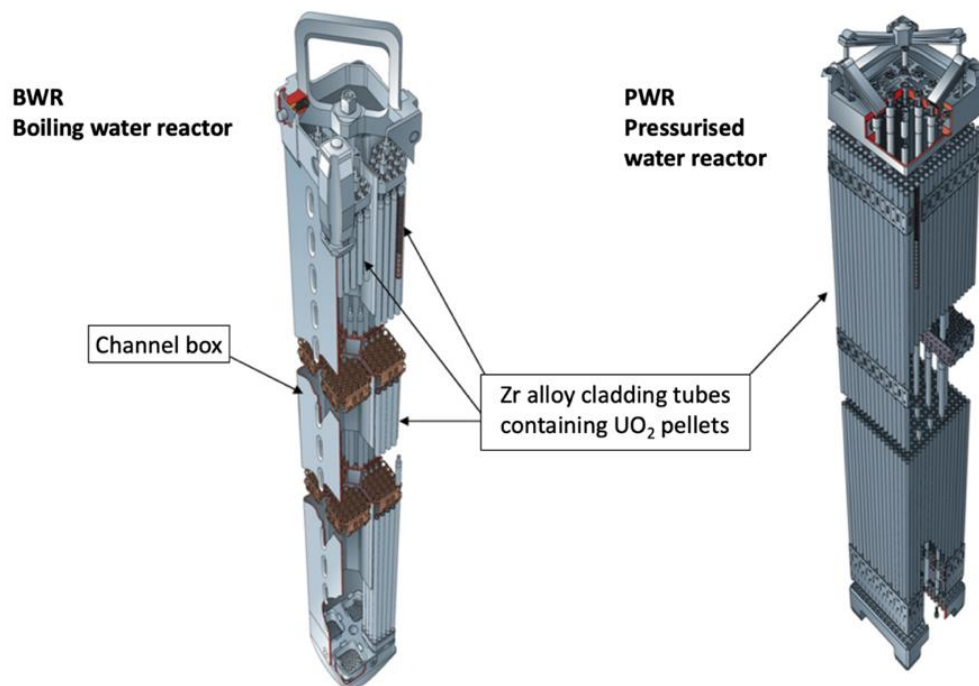


Figure 2.2: Schematic of fuel assemblies for BWRs and PWRs. Adapted from [16]. Reprinted with permission from Elsevier.



### 3. Zr alloy nuclear fuel claddings

A number of different Zr alloys are used for nuclear fuel claddings. In this chapter, some of the most common are mentioned, and some of the basics of crystallography, chemistry (with emphasis on the Zircalloys), manufacture, and texture of Zr alloys are described.

#### 3.1 Types of alloys

The main reference for this section is [11]. Additional references are stated in the text.

Zr alloys have been used as nuclear fuel cladding since the 1950s, their low absorption cross section for thermal neutrons being their main advantage [17]. Various types of Zr alloys have been developed over the years. In PWRs of non-Russian design, Zircaloy-4 has historically been the most common, but nowadays Nb-containing Zr alloys are generally used. In VVERs, Nb-containing Zr alloys have been used throughout most of their history. This is also the case for RBMKs (graphite-moderated, light-water-cooled reactors of Russian design) and CANDU reactors (heavy water reactors of Canadian design). CANDU reactors also use Zircaloy-2 and Zircaloy-4 for some components. Examples of Nb-containing alloys are ZIRLO™, Optimized ZIRLO™, M5® (all three used in PWRs), E110, E125, E635 (all three used in reactors of Russian design), and Zr-2.5Nb (used in CANDU reactors). In BWRs, Zircaloy-2 has been and still is the most common Zr alloy. HiFi™ and Ziron™ are two newly developed BWR claddings that have a slightly higher Fe content than Zircaloy-2 [18]. The higher Fe content results in lower HPU compared with Zircaloy-2 [18]. For channel boxes in BWRs, Nb-containing Zr alloys are often used in modern fuel assemblies [18]. Table 3.1 shows the typical composition of some of the most common Zr alloys.

Table 3.1: Content of alloying elements (wt%) in some of the most common Zr alloys. O is usually also present as an alloying element, not always within a specified range but typically below 0.2 wt%.

Alloy	Sn	Fe	Cr	Ni	Nb
Zircaloy-2 <sup>1</sup>	1.20–1.70	0.07–0.20	0.05–0.15	0.03–0.08	-
Zircaloy-4 <sup>1</sup>	1.20–1.70	0.18–0.24	0.07–0.13	-	-
ZIRLO <sup>2</sup>	0.9–1.2	0.1	-	-	0.9–1.13
Optimized ZIRLO <sup>3</sup>	0.6–0.79	0.09–0.13	-	-	0.8–1.2
M5 <sup>2</sup>	-	0.015–0.06	-	-	0.8–1.2
E110 <sup>2</sup>	-	0.006–0.012	-	-	0.95–1.05
E125 <sup>4</sup>	-	-	-	-	2.20–2.60
E635 <sup>2</sup>	1.10–1.30	0.30–0.40	-	-	0.95–1.05
Zr-2.5Nb <sup>1</sup>	-	-	-	-	2.50–2.80
HiFi <sup>5</sup>	1.5	0.40	0.10	0.08	-
Ziron <sup>5</sup>	1.46	0.26	0.10	0.05	-

<sup>1</sup>Values from [19].

<sup>2</sup>Values from [20].

<sup>3</sup>Values from [21].

<sup>4</sup>Values from [22].

<sup>5</sup>Values from [18].

## 3.2 Crystallography

The main reference for this section is [11]. Additional references are stated in the text.

Solid Zr exists in two phases, a hexagonal close-packed (HCP)  $\alpha$  phase below and a body-centred cubic (BCC)  $\beta$  phase above 865 °C [11]. In thermal nuclear reactors, where the operating temperature is in the range 280–330 °C, Zr is in the  $\alpha$  phase. However, during accident conditions, the temperature can be so high that a phase transformation to the  $\beta$  phase occurs.

A primitive unit cell for the hexagonal lattice can be constructed by using two  $a$  axes ( $a_1$  and  $a_2$ ) and a  $c$  axis. The  $a$  axes are separated by an angle of  $120^\circ$  and lie in a plane that is perpendicular to the  $c$  axis. Often, a non-primitive unit cell is used to more clearly reveal the hexagonal structure. Then, a third  $a$  axis ( $a_3$ ) being  $\pm 120^\circ$  from  $a_1$  and  $a_2$  is usually employed. A primitive and a non-primitive hexagonal unit cell are shown in Figure 3.1. For  $\alpha$  Zr the lattice parameters are  $c = 0.515$  nm and  $a = 0.323$  nm, and the  $c/a$  ratio is 1.59, which is somewhat lower than the ideal  $c/a$  ratio of  $2\sqrt{2/3}$  ( $\approx 1.63$ ) for an HCP lattice [23]. There are two atoms in the primitive unit cell with coordinates  $000$  and  $2/3 \ 1/3 \ 1/2$  ( $a_1 a_2 c$ ) [23]. In HCP lattices, there are two octahedral and four tetrahedral interstitial sites per primitive unit cell (both of the octahedral and two of the tetrahedral sites are fully contained within the cell, and eight tetrahedral sites are shared with three other cells each) [23]. However, the configuration of interstitial atoms is often such that two atoms are associated with one lattice site. Taking this into account in modelling using empirical potentials, there are eight interstitial configurations, tetrahedral (T), octahedral (O), basal tetrahedral (BT), basal octahedral (BO), crowdion (C), basal crowdion (BC), split (dumbbell) (S), and basal split (dumbbell) (BS) in HCP lattices [24]. In addition to these configurations, there are according to density-functional theory (DFT) modelling four more configurations that could be stable [25]. These are  $C'$  and  $BC'$ , which can be formed by breaking the symmetry of C and BC, respectively, and PS and P2S, which can be formed by breaking the symmetry of S. Figure 3.2 shows the conventional interstitial configurations obtained using empirical potentials, and Figure 3.3 shows the additional configurations obtained using DFT modelling.

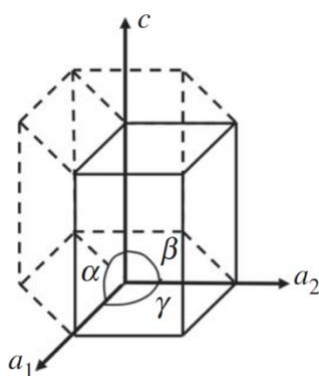


Figure 3.1: Primitive unit cell (solid lines) and non-primitive unit cell (dashed lines) of the hexagonal lattice.  $\alpha = \beta = 90^\circ$ .  $\gamma = 120^\circ$ . Reprinted with permission from The Royal Society (U.K.), [26].

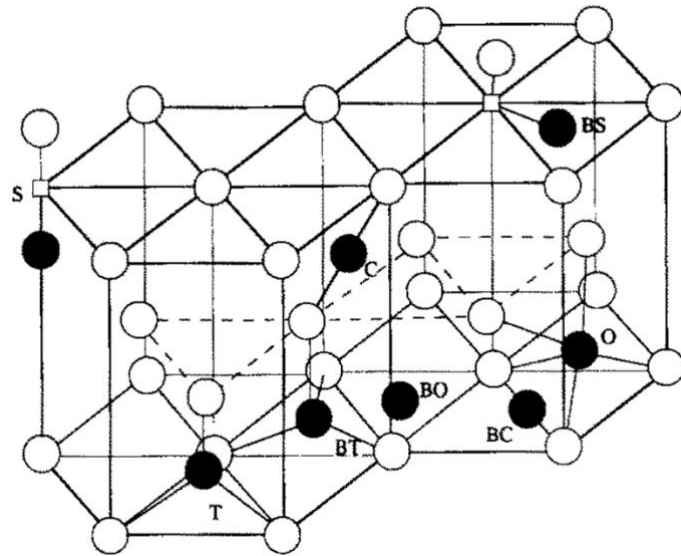


Figure 3.2: Interstitial sites in the HCP lattice. Reprinted with permission from Elsevier, [27].

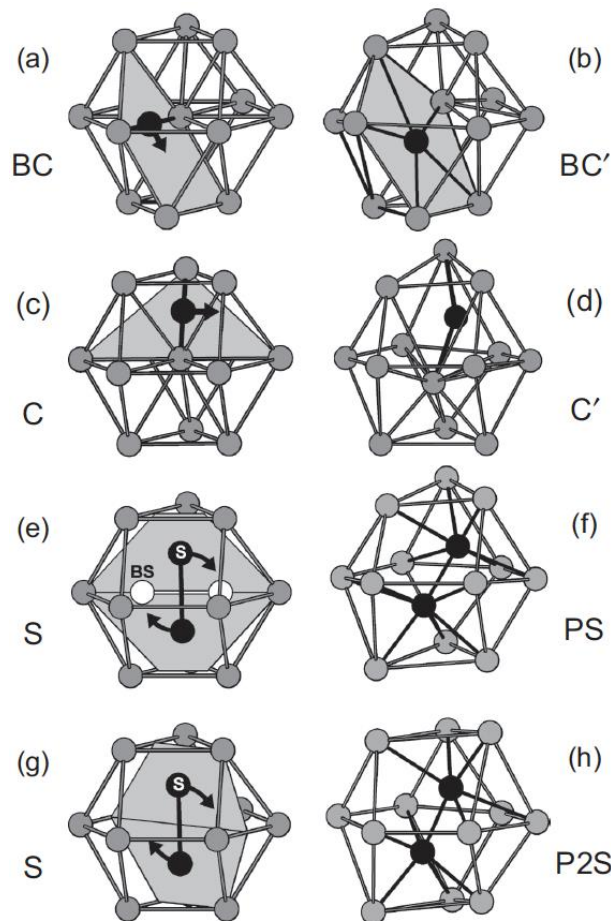


Figure 3.3: Low-energy interstitial sites formed by breaking the symmetry of the conventional interstitial sites in the HCP lattice. Reprinted with permission from the American Physical Society, [25].

Often, the hexagonal lattice system is described using the Miller–Bravais notation, a notation with four indices,  $(hkil)$ , where  $i = -(h + k)$  [28]. The third index,  $i$ , is thus redundant but used for convenience due to the symmetry. Indices within parentheses,  $(hkil)$ , denote families of

planes, indices within braces,  $\{hkl\}$ , denote all planes equivalent to the families of planes  $(hkl)$ , indices within square brackets,  $[hkl]$ , denote directions, and indices within angular brackets,  $\langle hkl \rangle$ , denote all directions equivalent to the directions  $[hkl]$ . In contrast to cubic lattices, directions in the hexagonal lattice are not always normal to the planes with the same indices. A number of atomic planes in the hexagonal lattice can be of interest when discussing radiation-induced defects. Figure 3.4 shows the basal, the first-order pyramidal, and the first-order  $\{10\bar{1}0\}$  and second-order  $\{11\bar{2}0\}$  prismatic planes together with the  $\langle c \rangle$  direction ( $[0002]$ ) and the  $\langle a \rangle$  directions ( $\langle 11\bar{2}0 \rangle$ ) of the lattice. For HCP lattices with a  $c/a$  ratio lower than  $\sqrt{3}$  ( $\approx 1.73$ ), such as Zr, the interplanar spacing is smallest for the  $(0002)$  planes, and for HCP lattices with a  $c/a$  ratio higher than  $\sqrt{3}$ , the interplanar spacing is smallest for the  $\{10\bar{1}0\}$  planes [29]. The stacking order of the  $(0002)$  planes is  $ABAB\dots$ , and the stacking order of the  $\{10\bar{1}0\}$  planes is  $ABCD A\dots$ , with the distance between A and B and between C and D equal to  $a\sqrt{3}/6$  and the distance between B and C and between D and A equal to twice this distance [30]. The pairs A–B and C–D are sometimes referred to as corrugated (first-order) prismatic planes, and the distance between these corrugated planes ( $= a\sqrt{3}/2$ ) is usually what is meant by the interplanar spacing of the  $\{10\bar{1}0\}$  planes. Figure 3.5 shows the stacking of the  $\{10\bar{1}0\}$  planes.

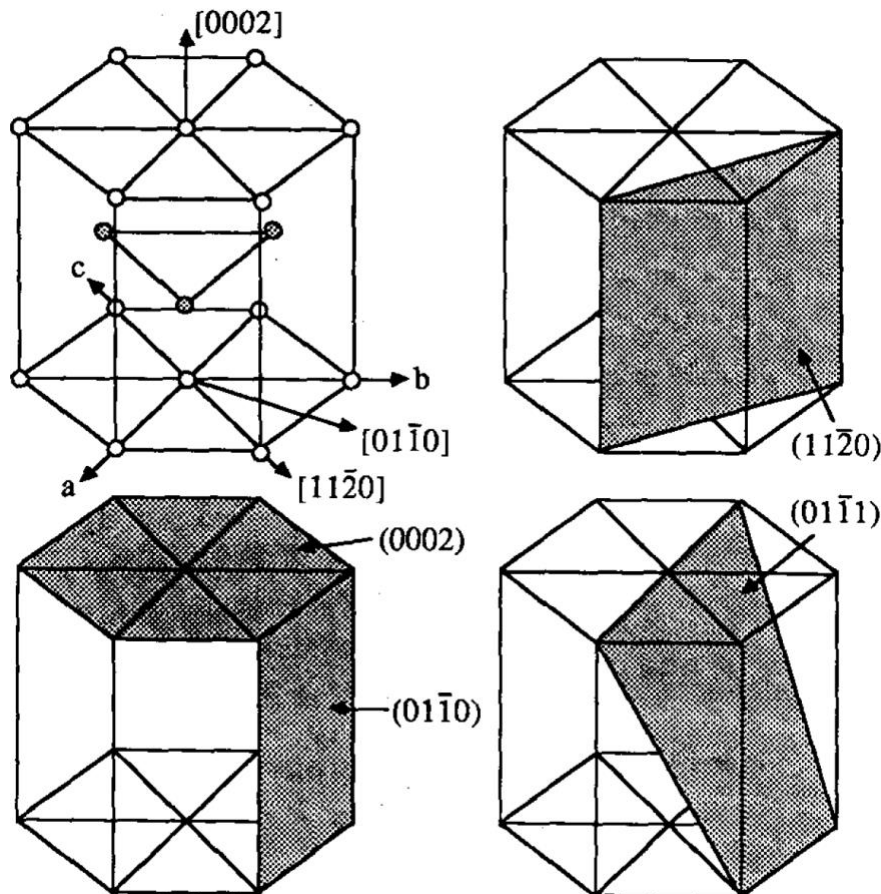


Figure 3.4: Directions and planes in the hexagonal lattice.  $a$ ,  $b$ , and  $c$  in the top left unit cell correspond to three of the  $\langle a \rangle$  directions (and thus correspond to the three  $a$  axes  $a_1$ ,  $a_2$ ,  $a_3$ ).  $[0002]$  indicates the  $\langle c \rangle$  direction.  $(11\bar{2}0)$  is a second-order prismatic plane,  $(01\bar{1}0)$  is a first-order prismatic plane,  $(0002)$  is the basal plane, and  $(01\bar{1}1)$  is a first-order pyramidal plane. Reprinted with permission from IEEE, [31].

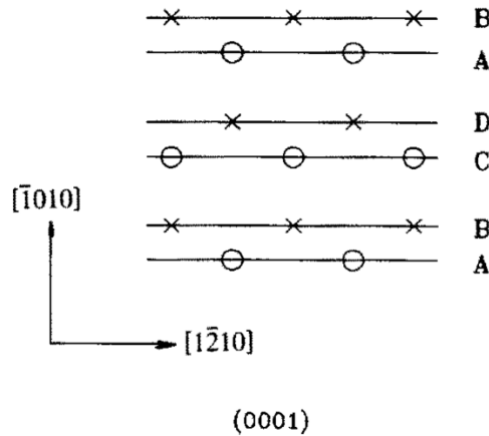


Figure 3.5: Stacking of prismatic planes in the HCP lattice. The circles correspond to the white and the crosses to the grey atoms in Figure 3.4. The pairs A–B and C–D are referred to as corrugated prismatic planes. Reprinted with permission from Elsevier, [30].

### 3.3 Chemistry

The main reference for this section is [11]. Additional references are stated in the text.

The alloy in focus of this study is Zircaloy-2. Its detailed composition range is shown in Table 3.2, together with the reason for adding each of the alloying elements. For comparison, the composition range of Zircaloy-4 is shown in the table. Zircaloy-4 contains no Ni. The reason for this is that HPU is decreased without the presence of Ni. In addition to the elements specified in Table 3.2, there are impurity levels of various elements present in the Zr alloys. Common impurities in Zircaloy-2 are C, N, Si, and Al [32,33].

Table 3.2: Composition of Zircaloy-2 and Zircaloy-4 (wt%) and the role of each alloying element. Values from ASTM Standard B350/B350M [19].

Element	Zircaloy-2	Zircaloy-4	Role of alloying element
Sn	1.20–1.70	1.20–1.70	Increases yield strength and corrosion resistance
Fe	0.07–0.20	0.18–0.24	Increases corrosion resistance
Cr	0.05–0.15	0.07–0.13	Increases corrosion resistance
Ni	0.03–0.08	-	Increases corrosion resistance
Fe + Cr + Ni	0.18–0.38	-	
Fe + Cr	-	0.28–0.37	
O	To be specified on order	To be specified on order	Increases yield strength

The solubility of Fe, Cr, and Ni is low in Zr. In the Zircaloys, second phase particles (SPPs) of the types  $Zr_2(Fe,Ni)$  and  $Zr(Fe,Cr)_2$  are formed. The  $Zr_2(Fe,Ni)$  SPPs (in Zircaloy-2) have been observed to be fewer in number and generally larger than the  $Zr(Fe,Cr)_2$  SPPs [34–38]. Also Si can be found in the SPPs [33]. O and Sn are  $\alpha$  stabilisers and do not form SPPs. Fe, Cr, and Ni are interstitial diffusers, and their diffusivity is about three times faster in the  $\langle c \rangle$  direction than in the  $\langle a \rangle$  direction of the Zr lattice. The diffusivities of Fe and Ni are higher than the diffusivity of Cr, and at temperatures of reactor operation the difference is several orders of magnitude [39]. Also O is an interstitial diffuser, and its diffusivity at temperatures of reactor operation is a few orders of magnitude lower than the diffusivity of Cr. Sn, as well as Nb, is a substitutional diffuser with slower and more isotropic diffusion [39].

### 3.4 Manufacture and texture

The main reference for this section is [11]. Additional references are stated in the text.

In Zr alloy manufacture, the starting material is usually ore containing both Zr and Hf. Due to the high thermal neutron capture cross section of Hf, a separation of the two elements is performed. The Zr is purified further before being mixed with the alloying elements and melted to form ingots. The thermal treatments and mechanical processing performed after this step vary between different alloys and different applications but usually comprise high-temperature forging or rolling in the  $\beta$  phase (at 1000–1050 °C), extrusion (for tubes) in the  $\beta$  phase, water-quenching from the  $\beta$  phase, intermediate-temperature forging and rolling (for sheets) or extrusion (for tubes) in the upper  $\alpha$  phase, and a number of low-temperature rollings or pilgerings with intermediate annealings. During treatment in the  $\beta$  phase, the SPPs are dissolved, the material is homogenised, and large grains are formed. Upon quenching, a basketweave structure of  $\alpha$  grains forms with SPPs at the grain boundaries. The succeeding processing steps lead to a more homogeneous distribution of SPPs. The annealings between the low-temperature processing steps are performed to increase the ductility of the final product. A fully recrystallised (RXA) product with equiaxed grains and SPPs both inside the grains and at the grain boundaries can be obtained. If the temperature of the final annealing step is decreased, a stress-relieved (SRA) product with elongated grains and improved mechanical properties can be obtained. It is also possible to get a partly recrystallised (PRXA) structure.

The crystallographic orientation of the grains in the final fuel cladding tubes is strongly anisotropic. The  $\langle c \rangle$  direction of the matrix is preferentially oriented approximately  $30^\circ$  from the radial direction of the tube, and one of the directions  $\langle 1\ 0\ -1\ 0 \rangle$  and  $\langle 1\ 1\ -2\ 0 \rangle$  is in or close to the axial direction [40]. Figure 3.6 shows the typical texture of Zr alloy cladding tubes.

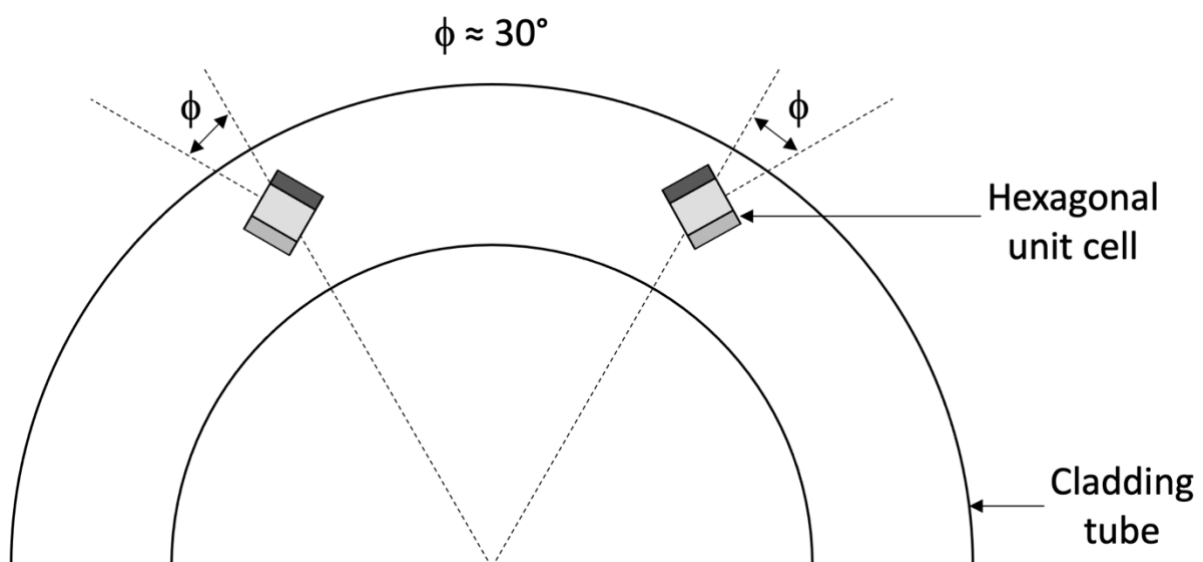


Figure 3.6: Schematic of the typical cladding tube texture.

## 4. Irradiation effects on Zr alloys

The radiation during reactor operation degrades the Zr alloys. This chapter describes the creation of point defects and dislocation loops, irradiation growth and irradiation creep, radiation-induced SPP dissolution, and pellet–cladding interaction.

### 4.1 Point defects and dislocation loops

The main references for this section are [11,41]. Additional references are stated in the text.

In a nuclear reactor, radiation damage in the Zr alloys is primarily caused by fast neutrons knocking out atoms from their lattice positions. For this interaction to occur, a minimum neutron energy is needed. This energy is different for different crystallographic orientations. A standard value of 40 eV is, however, commonly used as the energy needed to displace a Zr atom from its lattice position. This energy is very much smaller than the energy of the fast neutrons from the fission process ( $> 1$  MeV) but much larger than the energy of the thermalised neutrons (0.025 eV).

The first atom to be hit by the neutron and to be knocked out of its position is called the primary knock-on atom (PKA). After being knocked out, the PKA can displace other atoms, which in turn can displace other atoms, thus creating a collision cascade. The process of knocking out an atom from its lattice position creates a self-interstitial atom (SIA) and a vacancy, a so-called Frenkel pair. Most, but not all, Frenkel pairs recombine within the time frame of several picoseconds, and the resulting configuration of a cascade is considered to be a core of vacancies surrounded by interstitials [42]. Diffusion of the SIAs and vacancies that do not recombine affects the microstructural evolution of the material. In Zr and Zr alloys, the diffusion of SIAs has been proposed to be anisotropic with preferential diffusion in the basal plane, whereas the diffusion of vacancies has been proposed to be more isotropic [43,44]. This difference between SIAs and vacancies is termed diffusion anisotropy difference (DAD), and modelling using reaction kinetics and molecular dynamics indicates that this could explain parts of the microstructural evolution of Zr alloys [43,44]. However, more recent modelling using DFT, the kinetic Monte Carlo method, and rate theory indicates that, at temperatures relevant to reactor operation, vacancies instead diffuse more anisotropically than SIAs, both species diffusing preferentially in the basal plane [45]. If the more recent modelling is correct and the DAD model is invalid, some of the phenomena that could have been explained by DAD could instead be explained by formation and anisotropic diffusion of small SIA clusters [45,46].

Due to the high neutron flux and the continuous creation and recombination of Frenkel pairs during reactor operation, each individual Zr atom is displaced multiple times. Often, the average number of displacements per atom (dpa) is used to describe the radiation effect on materials. The neutron spectrum varies significantly for different types of reactors, and the neutron fluence is different for different positions in the reactor core. Therefore, individual dpa values have to be calculated for each position in each reactor. To get an approximate value, conversion factors from fast neutron fluence to dpa for PWRs and BWRs are 1.5–1.6 dpa/( $10^{25}$  n m<sup>-2</sup>) for a neutron energy  $E > 1$  MeV [47].

The SIAs and vacancies that do not recombine can be eliminated at defect sinks, e.g. grain boundaries and surfaces, or they can form clusters that can accumulate to form, e.g., small planar defects, either a piece of an extra atomic plane or a piece of a missing atomic plane. In

the first case a stacking fault due to interstitials is formed and in the second case a stacking fault due to vacancies is formed. Along the edge of a stacking fault a dislocation loop always exists. Dislocation loops in Zr and Zr alloys are commonly referred to as  $\langle a \rangle$  loops and  $\langle c \rangle$  component loops according to the direction of their Burgers vector,  $\mathbf{b}$ . The Burgers vector of a dislocation can be defined via comparing a closed circuit around a dislocation in a distorted lattice with a circuit taking the same number of steps in the same directions in an undistorted lattice where no dislocation is present. Since the lattice around the dislocation is distorted, the same circuit in the lattice without a dislocation will not be closed without an additional step. The length and direction of this step give the Burgers vector of the dislocation. Unfaulting (i.e. removal of the stacking fault) of dislocation loops can occur, leading to what is termed perfect dislocation loops [29]. For this to happen, the stacking fault energy, which increases with increasing loop size, needs to be so high that the perfect loop is energetically favourable. Loops that are associated with a stacking fault are referred to as faulted loops.

Vacancy  $\langle a \rangle$  loops are considered to be formed by condensation of vacancies on two adjacent layers in the  $ABCD\ldots$  stacking of the  $\{1\ 0\ -1\ 0\}$  planes, as condensation of vacancies on only one plane would lead to a much higher stacking fault energy [30]. According to modelling, unfaulting of vacancy  $\langle a \rangle$  loops is energetically favourable somewhere in the approximate diameter range 3–5 nm [48].

$\langle a \rangle$  loops have Burgers vector with components only in the  $\langle a \rangle$  directions, and for the  $\langle a \rangle$  loops observed in neutron-irradiated Zr and Zr alloys  $\mathbf{b} = 1/3\langle 1\ 1\ -2\ 0 \rangle$  [49]. Both interstitial and vacancy  $\langle a \rangle$  loops have been observed to coexist in various ratios depending on irradiation conditions and with large grain-to-grain variations, and both types have been reported to be perfect loops [50]. The habit plane of  $\langle a \rangle$  loops is close to, but usually not exactly on, the first-order prismatic plane; they have been observed to be distributed between the first- and second-order prismatic planes but with a tilt to the  $\langle c \rangle$  direction, meaning that their habit plane seems to be a pyramidal plane [51,52].  $\langle a \rangle$  loops are formed already after irradiation to low neutron fluence, and they align in layers that are parallel to the basal planes of the matrix [50]. The size of  $\langle a \rangle$  loops varies with irradiation temperature and is smaller in Zr alloys than in Zr without alloying additions [52]. After BWR exposure,  $\langle a \rangle$  loops in Zircaloy-2 have been observed to have a diameter of approximately 5 nm [53]. A transmission electron microscopy (TEM) micrograph of pure Zr showing  $\langle a \rangle$  loops aligned in layers perpendicular to the  $\langle c \rangle$  direction is shown in Figure 4.1, which also shows a schematic illustrating how  $\langle a \rangle$  loops (in a Zr alloy) are aligned on planes that are close to  $\{1\ 0\ -1\ 0\}$  and how they are imaged in TEM.

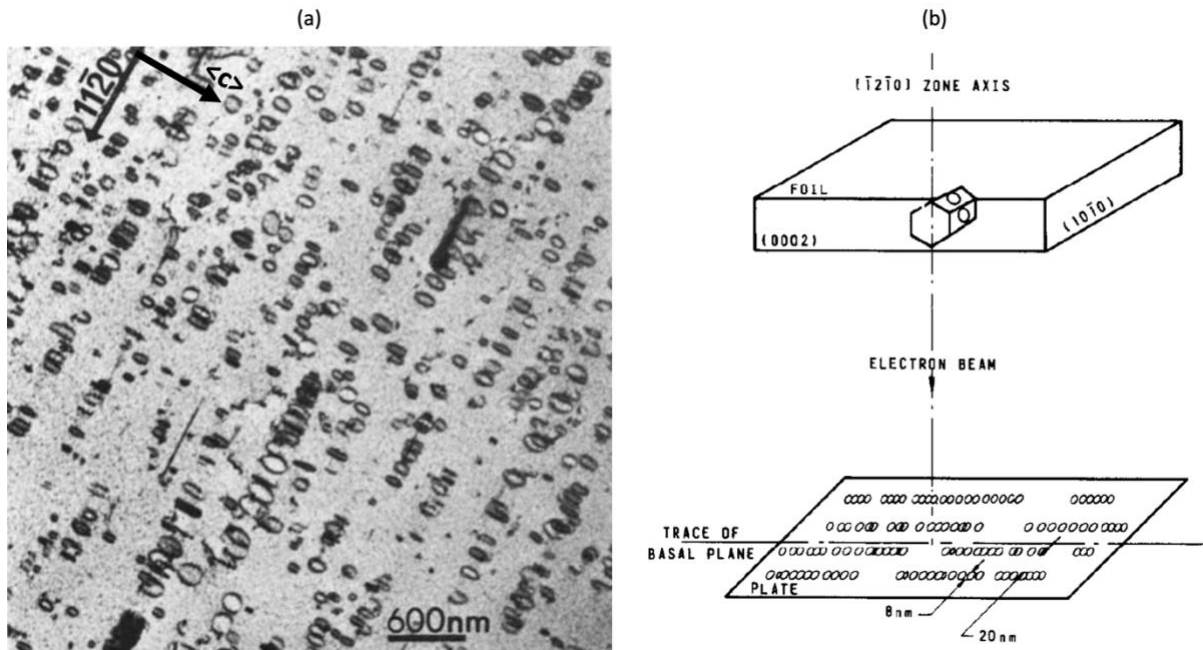


Figure 4.1: (a) TEM micrograph of  $\langle a \rangle$  loops aligned in layers perpendicular to the  $\langle c \rangle$  direction in neutron-irradiated pure Zr. The approximate  $[1\ 1\ -2\ 0]$  direction (one of the  $\langle a \rangle$  directions) and the approximate  $\langle c \rangle$  direction are indicated by the arrows. The negative beam direction was approximately  $[1\ -1\ 0\ 0]$ . Adapted from [50]. Reprinted with permission from Elsevier. (b) Schematic showing the alignment of  $\langle a \rangle$  loops on planes close to  $\{1\ 0\ -1\ 0\}$  in a Zr alloy and how the loops are imaged in the TEM. Reprinted with permission from Elsevier, [54]. The schematic in (b) is not drawn from the micrograph in (a), and therefore the loop size, the distance between loops, and the beam direction in (b) do not correspond to those in (a).

$\langle c \rangle$  component loops have Burgers vector with a component in the  $\langle c \rangle$  direction (with or without additional components in the  $\langle a \rangle$  directions), and for the  $\langle c \rangle$  component loops observed in neutron-irradiated Zr and Zr alloys  $\mathbf{b} = 1/6\langle 2\ 0\ -2\ 3 \rangle$  [49,55]. Only vacancy type  $\langle c \rangle$  component loops have been observed, and they have been reported to be faulted and inhabit the basal plane [49,55].  $\langle c \rangle$  component loops have been observed only after irradiation to high neutron fluence, in Zircaloy-2 after approximately  $3 \times 10^{25}\ \text{n m}^{-2}$ . Often,  $\langle c \rangle$  component loops can be observed close to dissolving SPPs. The size of  $\langle c \rangle$  component loops observed with TEM is approximately 100–1000 nm [49,53]. Alignment of  $\langle a \rangle$  loops has been suggested to be involved in the formation of  $\langle c \rangle$  component loops, and an anticorrelation of  $\langle a \rangle$  loop and  $\langle c \rangle$  component loop line density has been observed with TEM [53]. The atomistic mechanisms of  $\langle c \rangle$  component loop formation have been modelled in a number of studies, and from the results it seems that  $\langle a \rangle$  loops [56,57] or stacking fault pyramids [58] are involved in the formation. A schematic showing  $\langle a \rangle$  loops and  $\langle c \rangle$  component loops in relation to the hexagonal lattice is shown in Figure 4.2, and an APT reconstruction showing segregation of Fe to a  $\langle c \rangle$  component loop surrounded by clusters of Fe and Cr at expected positions of  $\langle a \rangle$  loops is shown in Figure 4.3.

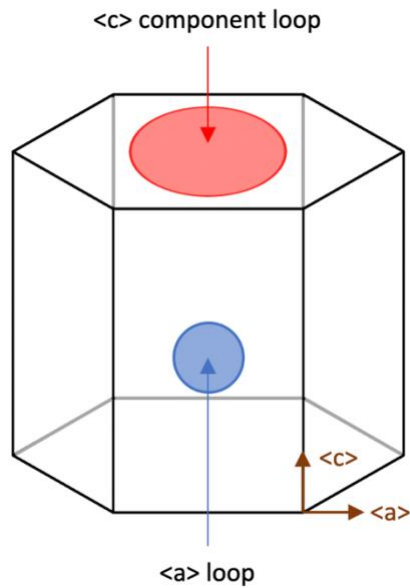


Figure 4.2: Schematic of the orientation of  $\langle a \rangle$  loops and  $\langle c \rangle$  component loops in relation to the hexagonal lattice. The  $\langle a \rangle$  loop in the schematic is located on a first-order prismatic plane, and the  $\langle c \rangle$  component loop is located on the basal plane.

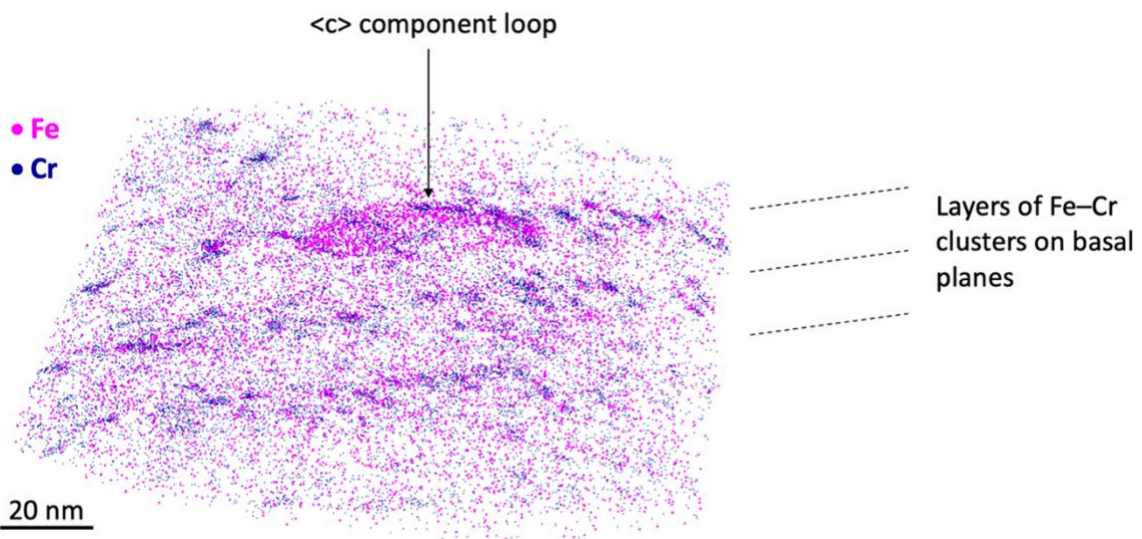


Figure 4.3: APT reconstruction of a  $\langle c \rangle$  component loop decorated with Fe and surrounded by clusters of Fe and Cr that probably are located at  $\langle a \rangle$  loops in Zircaloy-2 exposed to BWR operation.

## 4.2 Irradiation growth and irradiation creep

Zr alloys exposed to neutron irradiation undergo irradiation growth, which means that dimensional changes of unstressed material occur while the volume is unchanged [41]. The individual unit cells of the matrix expand in the  $\langle a \rangle$  directions and contract in the  $\langle c \rangle$  direction [41]. Since the texture of nuclear fuel cladding tubes is such that one of the  $\langle 1\ 0\ -1\ 0 \rangle$  or  $\langle 1\ 1\ -2\ 0 \rangle$  directions is in or close to the axial direction and the  $\langle c \rangle$  direction approximately  $30^\circ$  from the radial direction [40], the tube expands in the axial direction and contracts in the radial direction. Irradiation temperature, neutron fluence, amount of cold-work, texture, and material composition have been observed to affect the growth of Zr alloys

[5]. RXA material initially has a high growth rate for a short dose range, followed by a slow growth rate over a long dose range until a breakaway growth phenomenon occurs, meaning that the growth rate increases drastically [5]. Breakaway growth has been reported to coincide with the appearance of <c> component loops (i.e. at a fast neutron fluence ( $E > 1$  MeV) around  $3 \times 10^{25}$  n m<sup>-2</sup>) [59]. SRA material has a high growth rate from the onset of irradiation, comparable to that of breakaway growth in RXA material [5]. This is most probably due to the existence of <c> component loops in the as-produced SRA material [5]. The influence of alloying and impurity elements is not clear. Nb has been observed to delay the onset of <c> component loop formation, thereby delaying the onset of breakaway growth [5]. Increased Fe content seems to lead to decreased growth for some alloys [5,60,61]. Impurity levels of C should be kept below the solubility limit to minimise growth [5]. Also H picked up during operation can lead to increased growth [5,60].

The DAD model for vacancies and interstitials is able to explain the correlation between breakaway growth and the appearance of <c> component loops [43]. Also the more recent modelling not relying on DAD is capable of explaining this correlation [46,62,63].

Irradiation creep is deformation under irradiation in the presence of an external stress [41]. The total strain in the material can be taken as the sum of the creep strain and the growth strain (with the creep strain being due to both irradiation creep and thermal creep) [41]. In Zr alloys, the irradiation creep strain rate has been observed to vary with stress, irradiation temperature, neutron flux, amount of cold-work, dislocation density, content of alloying elements in solid solution, and grain size [5]. Creep seems to be dominated by diffusion under conditions of normal commercial reactor operation, but under some conditions, e.g. at low fluence and flux, dislocation slip can be the major contributor to creep [5]. The mechanisms behind growth and creep are connected, and it is thus generally not possible to separate growth from creep.

Irradiation growth and irradiation creep can lead to bowing of cladding tubes and channel boxes. This might lead to deteriorated flow conditions for the water in the core, problems with inserting control rods or control blades, and problems when handling fuel assemblies after operation [64]. Bowing occurs after the onset of breakaway growth [5]. As bowing is highly undesirable, reactors are operated in such a way that it is avoided.

### 4.3 SPP dissolution and alloying element redistribution

Under irradiation at temperatures of LWRs, Zr(Fe,Cr)<sub>2</sub> SPPs undergo transition from crystalline to amorphous. An amorphous rim forms at the periphery of the particles and progresses inwards towards the centre [11]. On the contrary, amorphous Zr<sub>2</sub>(Fe,Ni) SPPs have not been observed after irradiation at temperatures of LWRs [11]. After in-reactor exposure, preferential dissolution of Fe from the Zr(Fe,Cr)<sub>2</sub> SPPs has been observed. This has been evidenced by a decrease in the Fe/Cr ratio in the SPPs already after exposure to low fluence [35,65,66]. At fluences where there is a marked decrease in the Fe/Cr ratio in Zr(Fe,Cr)<sub>2</sub> SPPs, observations of no change in Fe/Ni ratio in the Zr<sub>2</sub>(Fe,Ni) SPPs have been made, indicating either absence of dissolution or simultaneous dissolution of Fe and Ni [35,66,67]. After exposure to high fluence, however, Fe has been observed to be preferentially dissolved also from the Zr<sub>2</sub>(Fe,Ni) SPPs [35,66,68]. A large fraction of the SPPs is dissolved during reactor operation, leading to a decrease in their number density [66]. Furthermore, the average SPP size has been observed to increase during reactor operation due to complete dissolution of small SPPs [66]. Since dissolution of the Zr(Fe,Cr)<sub>2</sub> SPPs starts at

a lower neutron fluence than  $Zr_2(Fe,Ni)$  SPPs, the  $Zr_2(Fe,Ni)$  SPPs dissolve later in life than  $Zr(Fe,Cr)_2$  SPPs, meaning that there are relatively more Ni-containing SPPs after exposure. The larger size of  $Zr_2(Fe,Ni)$  SPPs in the initial material also contributes to their relative increase in number density after irradiation.

The Fe, Cr, and Ni atoms that have been dissolved from the SPPs during reactor operation have been observed to cluster at positions of  $\langle a \rangle$  loops and segregate to  $\langle c \rangle$  component loops [35,53,69,70]. The observed clusters contain mainly Fe and Cr or Fe and Ni, but usually not Cr together with Ni [53,69,70]. Observations of clusters of Sn in regions where clusters of Fe and Cr are virtually absent and segregation of Sn to features interpreted to be  $\langle c \rangle$  component loops have been made with APT [69]. With TEM, Sn enrichment has been observed between layers clusters of Fe and Ni at  $\langle a \rangle$  loop dislocations [53]. Also, segregation of Sn, Fe and Cr to grain boundaries has been observed with APT [69,70], and with TEM Sn, Fe, and Ni have been observed at grain boundaries [71]. Overall, there are large grain-to-grain variations in the chemistry of irradiated Zircalloys [69,70,72].

#### 4.4 Pellet–cladding interaction

The main reference for this section is [73]. Additional references are stated in the text.

Pellet–cladding interaction (PCI) is interaction between the inside of the Zr alloy cladding and the fuel pellets. (Sometimes the term pellet–cladding mechanical interaction (PCMI) is used when mechanical interaction specifically is referred to.) The generation of thermal energy and the release of gaseous fission products inside the pellets during reactor operation lead to swelling and a change in shape of the pellets to an hourglass-like structure. Cracking of the pellets accompanies this change in shape. The cladding experiences creep due to the radiation and the pressure from the coolant water, and contact between the cladding and the pellets results. This means that the initial gap between the pellets and the cladding is closed. Usually, contact between cladding and pellet occurs after about a year of reactor operation in PWRs and after about two years in BWRs.

PCI can lead to cladding failure, especially in combination with stress corrosion cracking induced by corrosive fission products, of which iodine is considered to be the most prominent, and caesium and cadmium are considered to be possible contributors. Since the swelling of the fuel increases with increasing maximum power and the rate at which the power is changed, reactors are operated in such a way that PCI is avoided. Cladding failure due to PCI has not been much of a problem in PWRs but has historically been so in BWRs. To mitigate this problem, modern BWR claddings (since the 1980s) are manufactured with a Zr liner (making up about 10 % of the total wall thickness [74]) on the inside of the tubes. The liner is softer than the outer part of the cladding and has a different chemical composition. It is thus more resistant to cracking initiated by PCI. The bonding between the liner and the outer part of the cladding is metallurgic [74]. Low concentrations of alloying additions, e.g. Sn and Fe, are generally used in modern liners to increase the corrosion resistance in case the cladding is penetrated so that water can reach the inside of the tubes [18]. If a pure Zr liner is used, the risk of severe secondary degradation that leads to substantial amounts of radioactive substances being released to the coolant is increased [18].

## 5. Corrosion of Zr alloys

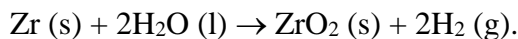
Corrosion degrades the Zr alloys during reactor operation. In this chapter, corrosion in autoclave and in reactor is described, and the effects of SPPs, alloying elements, and impurities are emphasised.

### 5.1 General corrosion phenomena in autoclave and in reactor

The main reference for this section is [75]. Additional references are stated in the text.

Corrosion of the fuel cladding is highly affected by the environment in the reactor. Minimising the corrosion and the HPU resulting from corrosion is the reason for utilising different types of Zr alloys in different types of reactors. On the outside of the oxide, a layer of crud, i.e. deposition of corrosion products from materials (e.g. stainless steel and Ni-base alloys) in the surroundings, is formed. If the oxide or crud layer gets too thick, the temperature of the cladding will increase, leading to an increase in the corrosion rate, leading to a further increase in oxide thickness. Such a positive feedback can result in both decreased mechanical properties and through-wall corrosion of the cladding tubes. The lower the corrosion rate, the higher the burnup of the fuel that is possible to achieve while still keeping a sufficient margin to cladding failure due to corrosion.

The oxide formed in the corrosion process is  $ZrO_2$ , zirconia. It exists (in addition to a high-pressure orthorhombic phase) in the three polymorphic forms, monoclinic, tetragonal, and cubic [76], whereof the two first are relevant for conditions of reactor operation. The overall reaction for formation of  $ZrO_2$  in water is



Since the diffusion of O is faster than the diffusion of Zr through zirconia, the oxide is inwards growing, meaning that the formation of zirconia takes place at the metal/oxide interface [11]. The transport path of O is nowadays considered to be via grain boundaries in the oxide [77], in contrast to a previously assumed vacancy-mediated mechanism [11]. As the Pilling–Bedworth ratio, the ratio of the volume of the oxide to the volume of the metal, is 1.56 for Zr, there is a volume expansion during growth of the oxide [11]. Usually, the oxide growth is measured as oxide thickness or as weight gain.

Based on autoclave corrosion, the corrosion can be described according to the following. In the initial stage of oxidation, the oxide thickness,  $d$ , is considered to be proportional to the oxidation time,  $t$ , raised to the power of  $n$ ,

$$d \propto t^n,$$

where  $n$  typically is around 1/3 [78].

At this stage of oxidation, the oxide is black (because of localised surface plasmon resonances in SPPs in the oxide [79]), protective, and consisting of small equiaxed grains. Columnar grains form and start to grow with their long axis perpendicular to the metal/oxide interface. Eventually, a transition occurs when the columnar grains become unstable (at a height of approximately 2  $\mu\text{m}$ ) due to compressive stresses, and small equiaxed grains start to grow at the metal/oxide interface. Below this layer, a new layer of columnar grains of

zirconia starts to grow, and the corrosion process continues according to this cyclic behaviour, forming a structure with alternating layers of equiaxed and columnar grains [78], [80]. The time between these cyclic transitions becomes increasingly shorter, and eventually a linear oxide growth rate can be observed. The three growth regimes are referred to as pre-transition (cubic), transition or transitory, and post-transition (linear). Although the pattern is cyclic in the transitory regime, the corrosion kinetics after the first transition is sometimes approximated by a linear relationship between oxide growth and corrosion time. (The cyclic pattern was not recognised in early corrosion models [81].) The corrosion rate of different alloys is related to the length of the transition cycles, with shorter cycles for faster-corroding alloys. Longer cycles are related to a thicker and denser innermost oxide layer, termed barrier oxide layer, that offers a more difficult transport path for oxygen ions inwards towards the metal/oxide interface. A higher fraction of columnar grains in the barrier oxide layer is beneficial for the corrosion properties. The thickness of the barrier oxide layer has been observed not to be the same as the thickness of the pre-transition oxide or the average thickness of the oxide of the transitory cycles. The oxide outside the barrier layer is associated with more cracks and porosities. The growth regimes (based on autoclave corrosion) are schematically shown in Figure 5.1.

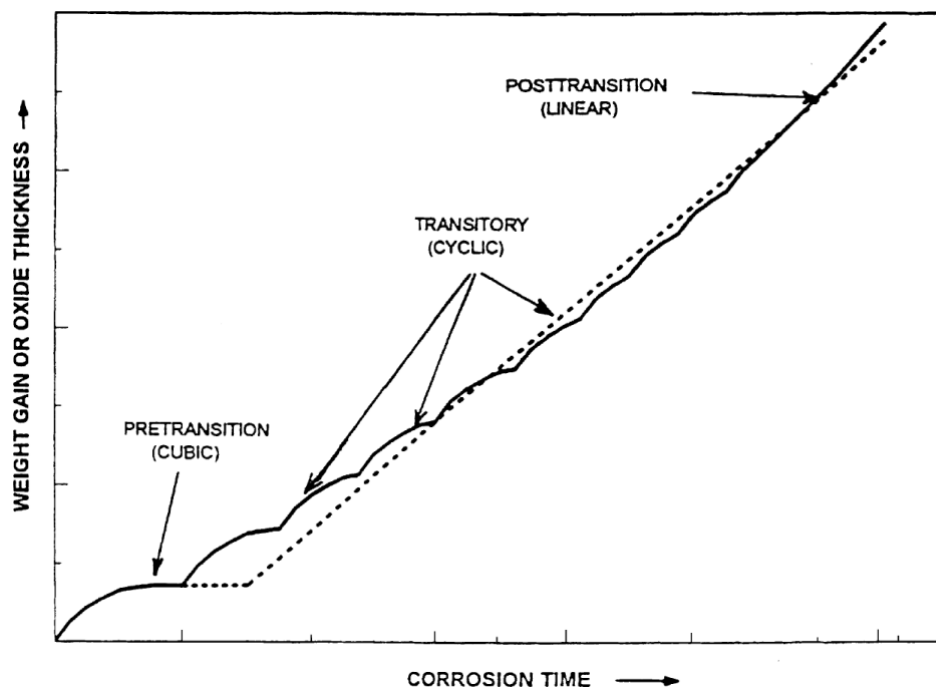


Figure 5.1: The three growth regimes of Zircaloy corrosion in autoclave. The dashed lines indicate earlier models that did not recognise the transitory regime. Reprinted with permission from Elsevier, [81].

In autoclave-corroded Zircalloys, a substoichiometric oxide layer of a few tens of nm with a composition close to  $ZrO$  forms at the metal/oxide interface and is followed by an O diffusion profile into the metal, extending up to some hundreds of nm, starting with saturated metal with about 30 at.% O and ending with the O concentration of the metal matrix [82–84]. The metal/oxide interface is undulated and has in Zircaloy-2 after autoclave corrosion been reported to have a periodicity of approximately  $1\ \mu\text{m}$  with an amplitude of 100 nm [83]. Lateral cracks in the oxide have been observed to preferentially form in the oxide above wave crests of the undulating metal/oxide interface and above SPPs [85]. Lateral cracks in the oxide have also been observed at positions corresponding to the cyclic transition interfaces between equiaxed and columnar grains [80]. The existence of cracks in the oxide has been

suggested to increase corrosion by facilitating inwards transport of oxygen ions through the oxide [80,85]. The growth of the oxide leads to the formation of subgrains in the metal close to the metal/oxide interface [86]. Figure 5.2 shows the metal/oxide interface and subgrains in the metal of autoclave-corroded Zircaloy-2.

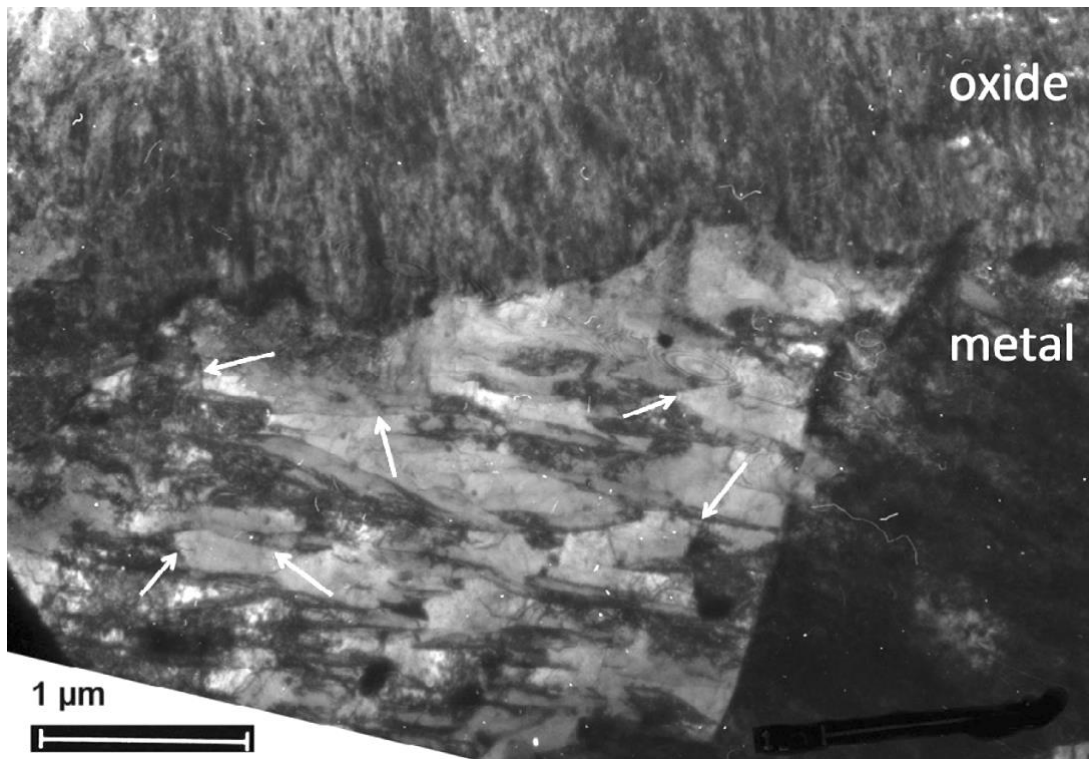


Figure 5.2: Metal/oxide interface in autoclave-corroded Zircaloy-2. Arrows indicate subgrain boundaries. Reprinted with permission from Elsevier, [86].

In reactor, the corrosion rate is usually enhanced compared with in-autoclave corrosion. This has for Zircaloy-2 been linked to the observation of a more heterogeneous oxide microstructure with weaker texture and more cracks compared with autoclave-corroded samples [87,88]. The number of cracks has been observed to increase with increasing exposure, and at the metal/oxide interface the cracks in the oxide have been observed to be located at or close to hydride phases in the metal [88,89]. Also after in-reactor exposure, the cyclic pattern of cracks in the oxide has been observed [80]. The enhanced diffusion resulting from interaction between fast neutrons and the oxide seems not to affect the corrosion rate, but dissolution of alloying elements from SPPs due to radiation seems to have large impact on corrosion [78].

If the environment is oxidising, as in BWRs, a phenomenon called shadow corrosion can occur when Zr alloys are in direct contact with or close to other metals and alloys. A difference in corrosion potential between Zr and the other material can lead to galvanic corrosion, resulting in increased oxide thickness at the affected Zr surface. Shadow corrosion has rarely led to fuel performance problems [75], but there is at least one example where enhanced shadow corrosion at spacer grids has done so [90]. Enhanced spacer shadow corrosion can occur when a cladding material with a small SPP size is used in a reactor with a low Fe/(Zn + Ni) ratio in the coolant [18]. To avoid this problem, the SPP size has been optimised [18].

## 5.2 Effects of SPPs, alloying elements, and impurities

The main reference for this section is [75]. Additional references are stated in the text.

The influence of SPPs and alloying elements on corrosion is not well understood. Some of the observations reported in the literature are summarised in this section.

In BWRs, nodular corrosion, i.e. corrosion localised to spots on the cladding tubes, has been a problem. It occurs in oxidising environments when the SPP size is large. By decreasing the average SPP size, the issue with nodular corrosion in BWRs has been resolved. In PWRs, where nodular corrosion has not been a problem, the SPP size has not been decreased, since smaller SPP size leads to an increase in uniform corrosion rate. Due to the dissolution of SPPs, a too small SPP size might be a problem also in BWRs. If the burnup of the fuel is to be increased, the increased neutron fluence exposure of the cladding will lead to more SPP dissolution, requiring a large SPP size to get good uniform corrosion properties during the whole operating life of the cladding. An optimisation of the SPP size is thus necessary to get both a low uniform corrosion rate and a low risk of nodular corrosion.

In autoclave corrosion, SPPs are known to be incorporated in unoxidised state into the oxide, both in unirradiated Zircaloy-4 and in Zircaloy-4 pre-irradiated with ions [91]. After being incorporated into the oxide, amorphisation of  $Zr(Fe,Cr)_2$  SPPs and preferential dissolution of Fe has been observed in the absence of irradiation. This effect of oxidation on SPP dissolution is similar to the effect of irradiation. Observation of enrichment of Fe and Ni at subgrain boundaries formed during autoclave corrosion has been observed both in the metal close to the metal/oxide interface and in the oxide [92].

Sn, which is added mainly to improve the mechanical properties of Zr alloys, is in BWRs beneficial also for the corrosion resistance. Especially the nodular corrosion is decreased by the presence of Sn. In PWRs, however, a decreased Sn content has been shown to improve the corrosion performance, and therefore the trend is that newly developed alloys for PWRs contain less Sn than many of the older alloys [93]. It is known that Sn is a stabiliser of tetragonal zirconia [94], and clusters and precipitates of Sn have been observed in the oxide of autoclave-corroded Zircaloy-2 [95]. In PWRs, Nb-containing alloys have lower corrosion rate than the Zircaloys [93,96].

Of the impurities in Zr alloys, N is the element that has the most detrimental effects on corrosion, both in autoclave and in reactor. Si has been observed to decrease the corrosion in reactor, whereas it in autoclave decreases the corrosion rate in concentrations below 120 (wt) ppm and increases the corrosion rate in concentrations above 120 ppm. C has been observed to increase corrosion in autoclave in the concentration range 100–300 ppm, to increase corrosion in PWR, and not to affect corrosion in BWR. Al has in autoclave been observed not to affect corrosion in concentrations up to 80 ppm and to increase corrosion in concentrations between 80 and 400 ppm.

## 6. H pickup and hydride phases in Zr alloys

HPU is a lifetime-limiting process in Zr alloys. As in the case of corrosion, the HPU varies significantly between different reactor types and different alloys. This chapter describes the origin of the H picked up, the influence of alloying elements on HPU, the solubility of H in Zr, and the Zr hydride phases.

In the overall corrosion reaction described in section 5.1, the H<sub>2</sub> gas formed in the splitting of the water molecules can be formed via positive H ions, H<sup>+</sup>, and H radicals, H<sup>•</sup> [75]. In addition to this, radiolytic dissociation of water molecules occurs, also producing H<sup>+</sup> and H<sup>•</sup> [8]. It has been proposed that, when not recombining to form H<sub>2</sub>, the H<sup>•</sup> species formed at the oxide/water interface can be transported through the oxide via hydroxylated grain boundaries and reach the metal [97]. The H<sub>2</sub> gas dissolved in the reactor coolant is thus not the hydrogen picked up by the Zr alloys. The H pickup fraction (HPUF) is used to quantify the HPU and is the amount of H picked up by the metal to the amount of H generated in the corrosion process.

HPU in binary Zr alloys has been studied out of reactor in [7]. From these results it seems that, compared with pure Zr, Sn has no impact on HPU, Fe and Cr decrease HPU, and Ni increases HPU. This can be seen in the commercial alloys, where the HPU in Zircaloy-2 is higher than in Ni-free alloys [75]. In BWRs, accelerated HPU in Zircaloy-2 is observed after a certain neutron fluence. This acceleration in HPU and HPUF is believed to be related to the dissolution of Zr<sub>2</sub>(Fe,Ni) SPPs and is followed by breakaway corrosion [67,75]. In Nb-containing Zr alloys, the HPU is relatively low [96,98]. The relatively lower HPUF of Nb-containing alloys compared with the Zircaloys has been suggested to be due to the presence of Nb<sup>5+</sup> in the oxide, which might lead to proton reduction at the oxide/water interface instead of at the metal/oxide interface [96].

When incorporated into the metal matrix, H atoms can occupy the tetrahedral and octahedral interstitial sites in the Zr lattice. According to DFT calculations, tetrahedral sites are preferred, with about 6 % of the H atoms located at octahedral sites at temperatures of reactor operation [99]. When the solubility limit is exceeded, hydride precipitation occurs [100]. The terminal solid solubility for precipitation differs from that for dissolution, and they are often denoted TSSP and TSSD, respectively. Results of measurements performed on Zircaloy-2 using differential scanning calorimetry [101], which correlate well with results obtained by other techniques [100], have yielded the following equations for TSSD and TSSP (for both unirradiated and irradiated material):

$$C_{TSSD} = 1.43 \times 10^5 \times \exp(-36\,686/(RT)), \quad (6.1)$$

$$C_{TSSP} = 3.27 \times 10^4 \times \exp(-25\,042/(RT)), \quad (6.2)$$

where  $C$  is the H concentration in (wt) ppm,  $R = 8.314 \text{ Jmol}^{-1}\text{K}^{-1}$  is the gas constant, and  $T$  is the temperature in K. This gives approximate terminal solid solubilities of 91 and 220 ppm at 600 K and of 0.059 and 1.4 ppm at 300 K for TSSD and TSSP, respectively. The solubility of H is thus much higher at temperatures of reactor operation, and therefore there are more hydrides in the cladding tubes post service. Irradiation effects have been observed to lead to increased H solubility, both experimentally [102,103] and by modelling [99]. Modelling also indicates that Fe, Cr, and Ni increase the H solubility, that O, Sn, and Nb do not affect the H solubility, and that all alloying elements destabilise hydride phases, meaning that hydride phases probably are less likely to form where the alloying elements are present [104].

There are four known hydride phases in Zr, with the following names and approximate stoichiometries:  $\zeta$  —  $\text{ZrH}_{0.5}$ ,  $\gamma$  —  $\text{ZrH}$ ,  $\delta$  —  $\text{ZrH}_{1.5-1.7}$ ,  $\varepsilon$  —  $\text{ZrH}_2$  [100].  $\delta$  and  $\varepsilon$  are stable phases,  $\zeta$  is metastable, and  $\gamma$  is probably a metastable phase that is stable only under certain conditions [100]. The crystallography of the hydride phases differs from the crystallography of the Zr matrix. However, the atomic positions of Zr are not very different in the hydride phases compared with  $\alpha$  Zr [99,105,106]. The crystal structures of the phases are trigonal for  $\zeta$  (which is fully coherent with  $\alpha$  Zr with a twice as large lattice parameter in the  $\langle c \rangle$  direction [107]), face-centred tetragonal (FCT) for  $\gamma$ , face-centred cubic (FCC) for  $\delta$ , and FCT for  $\varepsilon$  [100]. The  $\{111\}$  planes for the FCC and FCT phases correspond to the  $(0002)$  planes of the hexagonal  $\alpha$  Zr phase. Both  $\gamma$  and  $\delta$  hydrides have been observed to exist as plate-like structures in the Zr matrix. The habit plane, which corresponds to the broad side of the plate, has for both  $\gamma$  and  $\delta$  been observed to be parallel to  $\{1\ 0\ -1\ 0\}$  and  $\{1\ 0\ -1\ 7\}$  [100]. For  $\delta$ , a number of other habit planes also have been observed [100]. The growth direction of hydrides in the absence of external stresses is  $\langle 1\ 1\ -2\ 0 \rangle$ , and in the presence of external stresses, the growth direction is perpendicular to tensile stresses and parallel with compressive stresses [100]. Intergranular hydrides with their habit plane parallel with grain boundaries often form [100]. A Zr–H phase diagram is shown in Figure 6.1, the lattice parameters for the hydride phases and  $\alpha$  Zr are shown in Table 6.1, and unit cells for  $\gamma$ ,  $\delta$ , and  $\varepsilon$  hydrides are shown in Figure 6.2.

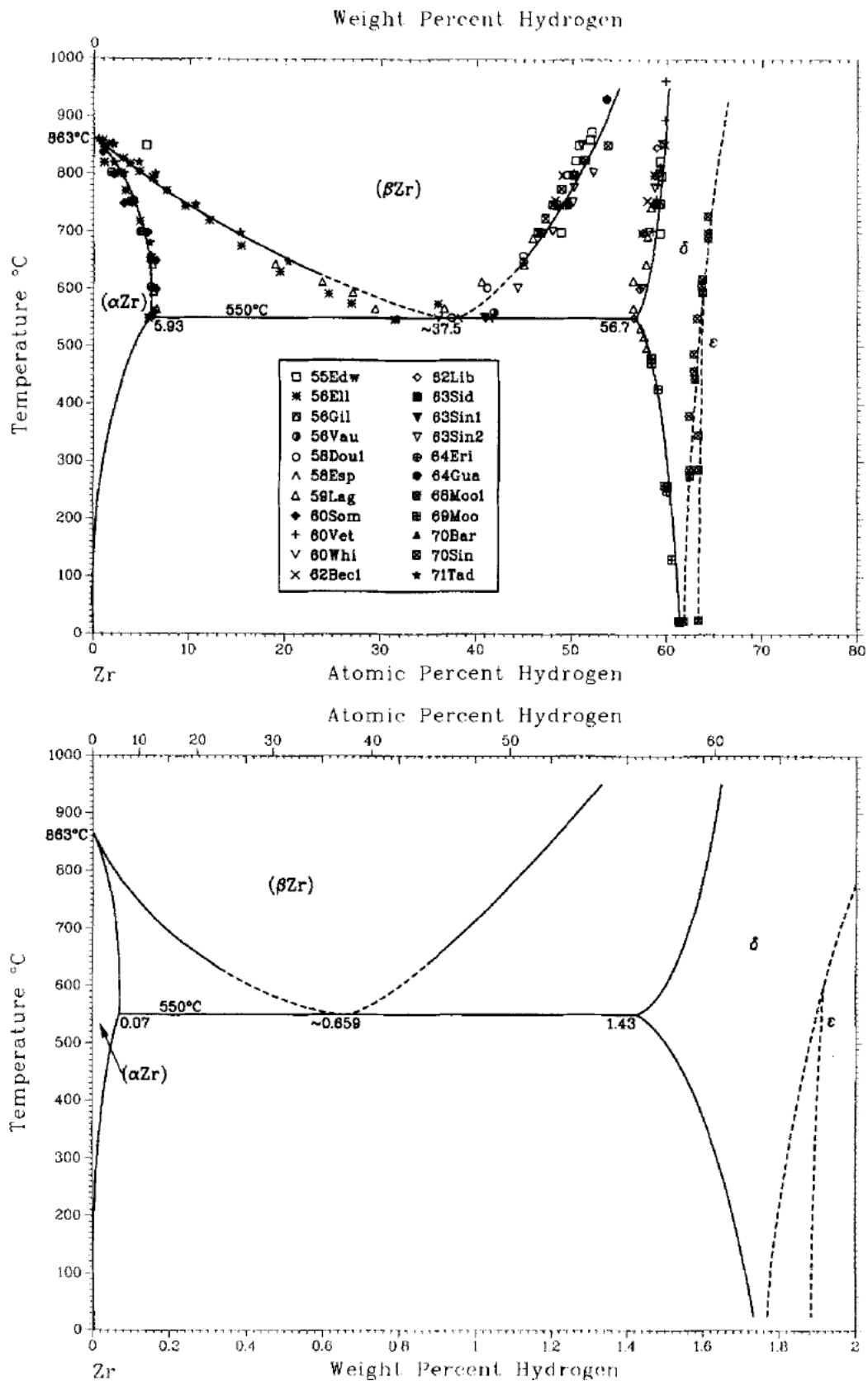


Figure 6.1: A Zr–H phase diagram. Top: with experimental data. Bottom: without experimental data. Reprinted with permission from Springer Nature, [108].

Table 6.1: Lattice parameters of  $\alpha$  Zr and the hydride phases in Zr.

Phase	Crystal structure	$a$ (nm)	$c$ (nm)
$\alpha$ Zr <sup>1</sup>	HCP	0.323	0.515
$\zeta$ <sup>2</sup>	Trigonal	0.33	1.029
$\gamma$ <sup>3</sup>	FCT	4.586	4.948
$\delta$ <sup>4</sup>	FCC	4.771	-
$\varepsilon$ <sup>5</sup>	FCT	4.975	4.447

<sup>1</sup> Values from [109].

<sup>2</sup> Values from [107].

<sup>3</sup> Values from [110].

<sup>4</sup> Value from [111].

<sup>5</sup> Values from [112].

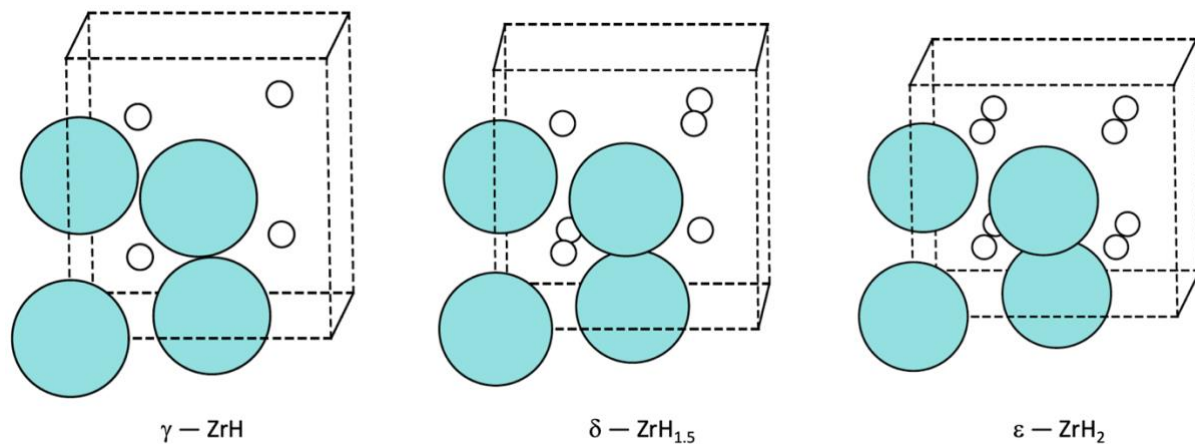


Figure 6.2: Unit cells for  $\gamma$ ,  $\delta$ , and  $\varepsilon$  hydrides. Adapted from [105]. Reprinted with permission from Springer Nature.

Since the diffusivity of H in  $\alpha$  Zr is high, the hydrides may be located far from where the H entered the metal [75]. The location and orientation of hydrides are highly dependent on the stresses in the metal [11]. The crystallographic texture of the cladding tubes determines the stress orientation, thus affecting the hydride orientation [11]. Tangential orientation of hydrides is beneficial for the mechanical properties of the cladding, whereas radial orientation leads to embrittlement and increased risk of delayed hydride cracking (DHC) [100]. Post service, when the cladding tubes are moved from wet storage to dry storage, the temperature in the cladding initially increases and subsequently decreases again. Many of the hydride phases are then initially dissolved followed by reprecipitation at the lower temperature. The hydride phases are thereby reoriented. This might lead to an increased risk of cladding failure if a larger amount of radial hydrides is precipitated. The phases that cause most cladding failures and, therefore, have been studied most are  $\delta$  and  $\gamma$  [100]. Also during sample preparation, e.g. for microscopy studies, the atomic configuration of H might be rearranged and hydride phases formed or dissolved [50,66,113,114].

## 7. Experimental techniques

The experimental technique used to acquire the data evaluated in this thesis is APT. This chapter describes the basic principles of this technique and methods of data evaluation along with normal procedures of specimen preparation. The main references for this chapter are [115–117]. Additional references are stated in the text.

### 7.1 Atom probe tomography

This section is divided into four subsections. The first gives an overview of APT, the second describes the procedures for specimen reconstruction and data evaluation, the third describes some limitations and common artefacts associated with APT, and the fourth describes APT of Zr alloys.

#### 7.1.1 Overview

APT is a destructive microscopic technique that offers resolution at the near-atomic scale. The specimen to be studied is needle-shaped with a tip diameter of some tens of nanometres and is subjected to a direct current (DC) positive electric field. Due to the small radius of the tip, the field at the surface is very high, several tens of V/nm. When subjected to a sufficiently high field, ionised atoms or molecules at the tip surface are evaporated, a process called field evaporation, and emitted from the specimen. As the evaporation probability depends on field strength and temperature, it is possible to achieve field evaporation by pulsing with either an additional electric field (voltage pulse mode) or a laser beam that heats the specimen (laser pulse mode). The penetration depth of the field is very low, and therefore only ions at the surface are evaporated. After being evaporated, the ions are accelerated by the electric field towards a position-sensitive detector, where a highly magnified image of the tip is created. The magnification is roughly  $L/R$ , where  $L$  is the flight path length and  $R$  the tip radius, and is typically  $10^6$ .

The time-of-flight for each ion depends on its mass-to-charge ratio. The time-of-flight is measured as the time between the evaporation pulse and the event of the ion hitting the detector. From this, a mass spectrum, showing the mass-to-charge ratio (usually in the unit Da) on one axis and the number of hits on the other, can be created. Thus, chemical information about the specimen is obtained. Since the impact position and the order of events at the position-sensitive detector are stored, it is possible to make a three-dimensional (3D) reconstruction of the specimen. Combining this 3D reconstruction with the chemical information obtained makes it possible to use APT for both spatial and chemical analysis at length scales ranging from atomic interplanar spacings to micrometres.

APT measurements have to be performed under ultra-high vacuum, typically in the range of  $10^{-8}$  Pa. Therefore, all APT instruments are equipped with a vacuum system. Most commonly, a local electrode, i.e. an electrode positioned at a distance on the order of tens of micrometres from the specimen apex, is utilised for accelerating the emitted ions towards the detector. The voltage used for the DC electric field is typically several kV, and it increases throughout the analysis as the specimen gets less sharp. The pulse frequency is usually in the range 100–500 kHz for both voltage and laser pulsing. Green lasers with pulse energies of 0.01–1 nJ or UV lasers with pulse energies about a factor 100 lower are commonly used. (Due to a difference in focus between green lasers and UV lasers, the energy per unit area is

not a factor 100 lower for UV lasers.) During analysis, the specimen is held at a temperature in the range 20–100 K. The material to be studied and the desired information from the study determine what values of the analysis parameters to use.

The flight path to the detector after leaving the local electrode is straight in instruments that are not equipped with a reflectron and curved in instruments that are equipped with a reflectron. A reflectron is a time- and space-focusing device that gives all ions of equal mass-to-charge ratio equal flight times to the detector by increasing the flight path length for ions of higher energy. This is done by an electrostatic field that deflects the ions entering the reflectron towards the detector. Ions of higher energy travel longer into the reflectron and thus take a longer path to the detector, which means that their time-of-flight is increased. Instruments with a reflectron have better mass resolution but slightly decreased spatial resolution compared with instruments without a reflectron. A schematic of APT and flight paths with and without reflectron is shown in Figure 7.1.

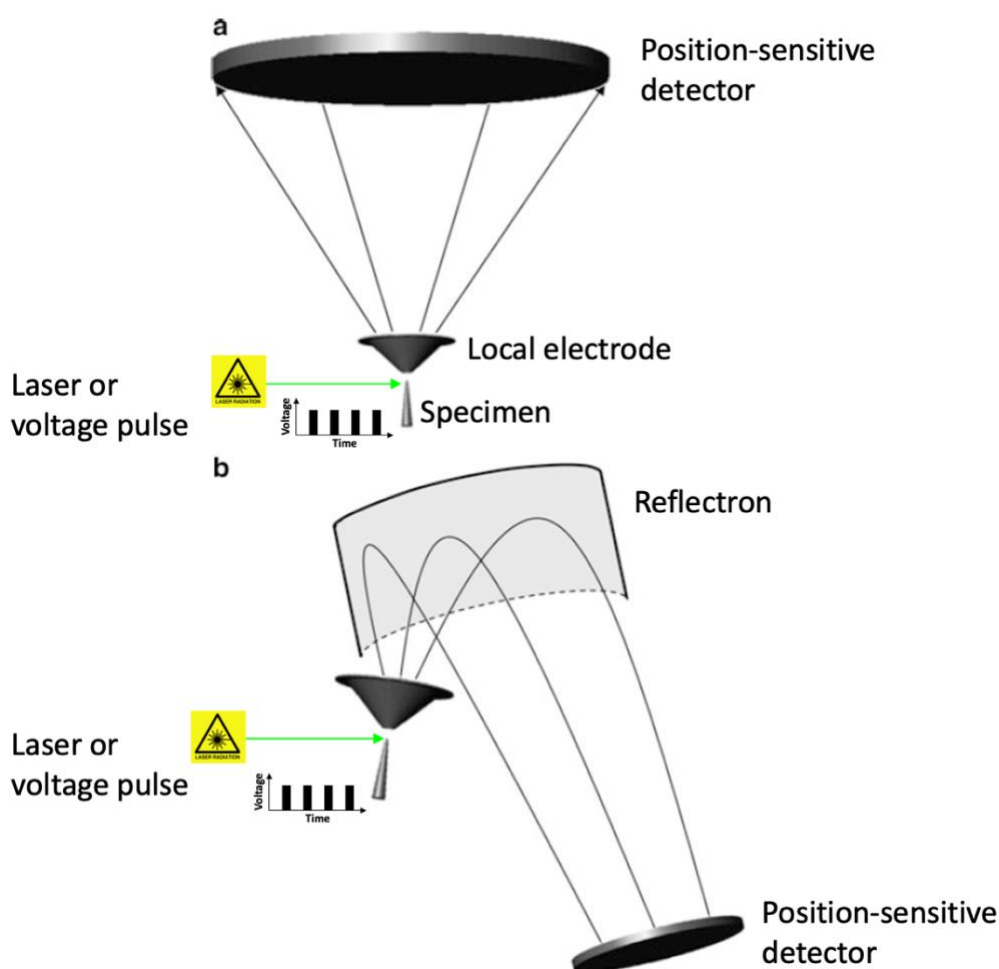


Figure 7.1: Schematic of APT. (a) Without reflectron. (b) With reflectron. Adapted from [116]. Reprinted with permission from Springer Nature.

### 7.1.2 Specimen reconstruction and data evaluation

There are a number of ways to reconstruct the specimen from the experimental raw data. Most of the reconstruction protocols commonly used are based on the Bas protocol [118]. The specimen apex is assumed to be hemispherical, and the evaporation is assumed to be uniform across the projected tip area. Reconstruction is done in the lateral directions for successive layers of evaporated species in the axial tip direction. Four parameters are used, the detection efficiency ( $\eta$ ), the evaporation field ( $F_e$ ), the field factor ( $k_f$ ), and the image compression factor ( $ICF$ ). The electric field,  $F$ , and the field factor are related to the radius of curvature  $R$  of the specimen tip and the combined voltage  $V$  of the DC electric field and the pulse according to

$$F = V/(k_f R). \quad (7.1)$$

During measurement, where  $V$  is adjusted to get a constant evaporation rate,  $F \approx F_e$ .

The image compression factor can be expressed as

$$ICF = \theta_{crys}/\theta_{obs}, \quad (7.2)$$

where  $\theta_{crys}$  is the crystallographic angle and  $\theta_{obs}$  the observed angle.  $\theta_{obs}$  is related to the distance  $D$  between observed crystallographic poles on the ion density map obtained during analysis and the flight path length  $L$  according to

$$\theta_{obs} = \arctan(D/L). \quad (7.3)$$

Normally, the image compression factor has a value between 1 and 2, where 1 corresponds to a radial projection and 2 to a stereographic projection. When the hemispherical surface of the tip cuts parallel lattice planes these take the shape of concentric rings on the surface. The centre of these rings is called a (crystallographic) pole. Poles can appear as a region of high, or low, density on the detector hit map.

It is usually difficult to calibrate the reconstruction. If crystallographic information is obtained in the analysis, that information might be used for determining appropriate values of  $k_f$  and  $ICF$ . Crystallographic poles can be visible on the detector hit map, see for example Figure 2 in Paper I. Sometimes, the poles can be identified using the symmetry on the hit map and, if multiple poles are visible, the distance between the poles on the hit map. Also, if there are features within the sample that have a known crystallographic orientation, these can be used for identification of the poles (or for identification of the crystallography if no poles are visible). At the poles, atomic planes are sometimes visible in the reconstruction. Using the atomic spacing of the different sets of planes and the angles between the planes of a known crystal structure it is possible to iteratively change the values of  $k_f$  and  $ICF$  to get an appropriate reconstruction. If only one pole with visible atomic planes is observed and identified, it is often possible to get a reconstruction that is appropriate regarding spacing of those planes but that does not necessarily give an appropriate representation of other crystallographic directions. However, crystallographic information is only occasionally obtained in APT analysis, and calibrations of the reconstruction according to the above are therefore usually not possible to perform. Complementary microscopy techniques such as field ion microscopy (FIM), TEM, transmission Kikuchi diffraction (TKD), and electron backscatter diffraction (EBSD) can in some cases be used to obtain additional information on

crystallography or other features in the specimen in order to calibrate the reconstruction or to enable interpretation of results. Alternatively, the specimen can after analysis be viewed using scanning electron microscopy (SEM) or TEM to measure  $R$  and thereby obtain a reasonable value of  $k_f$  (assuming the evaporation field is known).

When the reconstruction has been performed there is a variety of means to evaluate the data, the choice of which to use depends on what features are present in the specimen and what information about these features that is desired. Often, quantitative information about clusters of solute species is wanted. Multiple ways of obtaining this information exist. The definition of a cluster is not straightforward and can be done more or less arbitrarily. In the definition, clusters might not be distinguished from precipitates, and from APT data it is in many cases not possible to tell the difference between the two. Various algorithms are used for cluster characterisation, one of the most common being the maximum separation method (MSM) [119,120]. In this algorithm, the distance between detected species is used to define clusters. A minimum number,  $N_{min}$ , of solute species with a separation distance between individual species not exceeding  $d_{max}$  form a cluster. Other species within the envelope distance  $L$  from the solute species of the cluster can be included in the cluster. A halo of these other species might then form around the cluster. This halo is eroded away by applying an erosion step, removing species that are not the solute atoms of the cluster and that are located within the erosion distance,  $d_e$ , from species that are located outside of the cluster and are not of the same kind as the solute atoms of the cluster. The order of neighbours (i.e. first nearest neighbours, second nearest neighbours etc.) for which  $d_{max}$  is applied has to be specified. A schematic of MSM is shown in Figure 7.2.

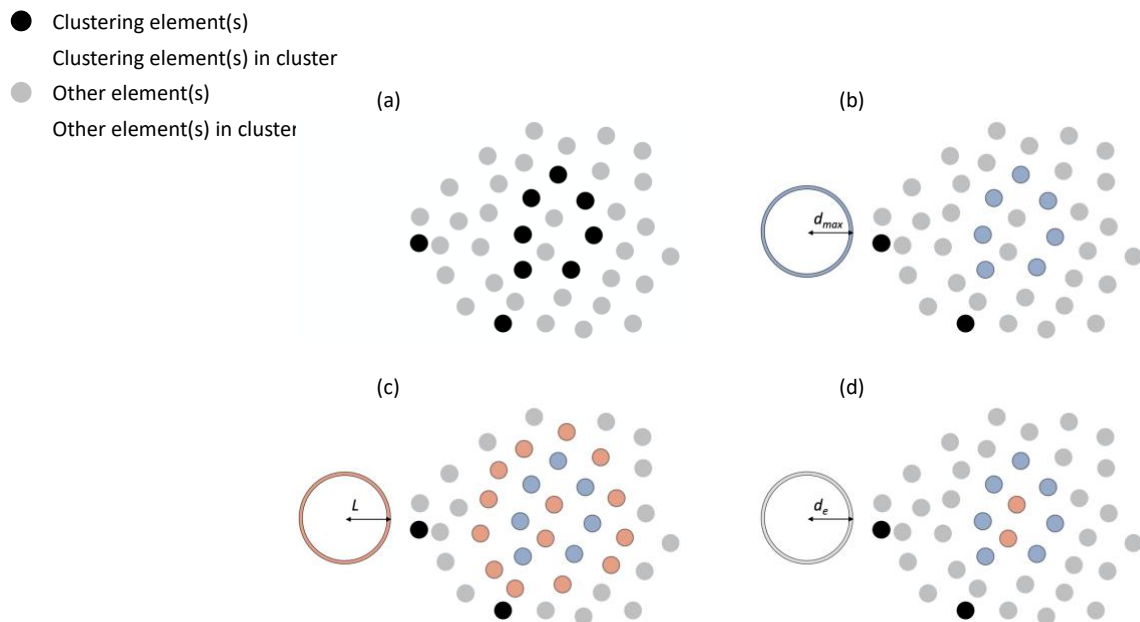


Figure 7.2: Schematic of cluster definition using the MSM. (a) Ions of clustering element(s) identified. (b) Ions of the clustering element(s) within  $d_{max}$  from other ions of the clustering element(s) belong to the cluster. (c) Other ions within  $L$  from the ions in the cluster are incorporated to the cluster. (d) Other ions within  $d_e$  from other ions than the clustering ions are eroded away from the cluster, thus defining a final cluster.

The values of the abovelisted parameters in the MSM algorithm are determined by the person performing the cluster analysis. A comparison with randomised distributions of the same composition and positions as the data to be evaluated can aid in the decision-making. Nearest neighbour distributions, cluster size distributions, and cluster count distributions are frequently used for this purpose. The nearest neighbour distribution shows the distance from species of interest to other species of the same type. When the average distance between the species of interest is shorter for the experimental data than for the randomised data, clustering is indicated. Clustering often, but not always, gives a bimodal distribution of the experimental data, with one mode for the clusters and one for the matrix. Nearest neighbour distributions can be determined for various orders of nearest neighbours. The cluster size distribution can be used to determine an appropriate value of  $N_{min}$  for a given value of  $d_{max}$ . It shows the number of clusters as a function of  $N_{min}$ . The cluster count distribution can be used to find an appropriate value of  $d_{max}$  for a given value of  $N_{min}$ . It shows the number of clusters as a function of  $d_{max}$ . Clustering is indicated by the number of clusters for small values of  $d_{max}$  being higher for the experimental data than for the randomised data. Iteration might be needed to find appropriate values of  $d_{max}$  and  $N_{min}$  from cluster count distributions and cluster size distributions. Figure 7.3 shows a nearest neighbour distribution and a cluster count distribution.

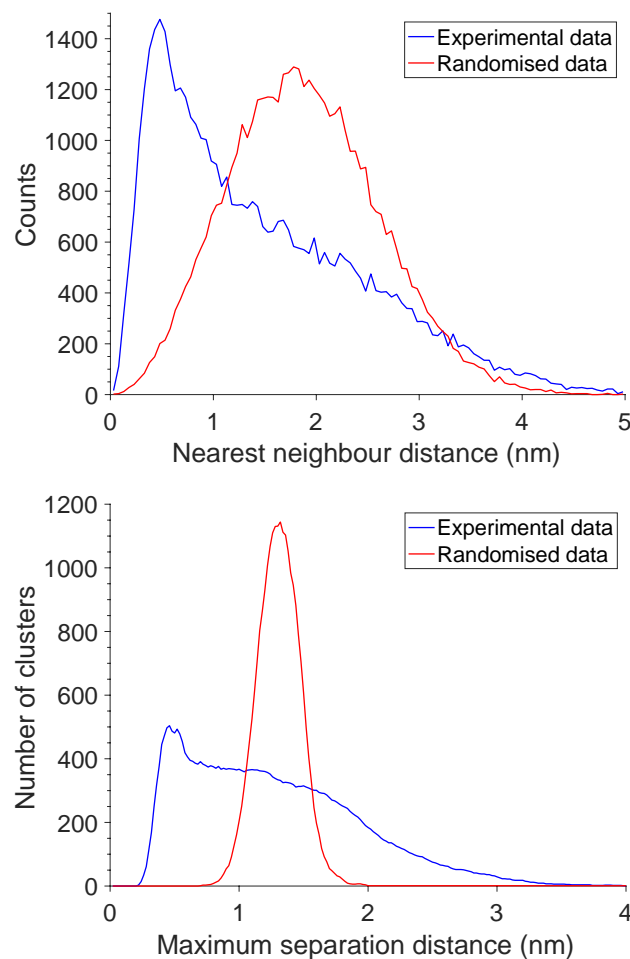


Figure 7.3: Nearest neighbour distribution (top) and cluster count distribution (bottom) for Fe and Cr in Zircaloy-2 exposed to BWR operation. Both distributions indicate a non-random arrangement of Fe and Cr, thus indicating clustering.

One other way of characterising clusters is by isoconcentration surfaces, which are the surfaces given by a specific concentration of one or more elements. From isoconcentration surfaces, proximity histograms, abbreviatedly called proxigrams, showing concentration as a function of distance from the surfaces, can be computed [121]. Isoconcentration surfaces and proxigrams can also be used for characterisation of other features than clusters, e.g. grain boundaries and phase boundaries.

Information that is often searched for in cluster analysis is number density, composition, and size. It might also be desirable to decide how the clusters are oriented with respect to the crystallography of the specimen. However, since crystallographic information is only occasionally obtained in APT analysis, it is most often not possible to determine the cluster orientation in relation to the crystallography. Compared with laser pulsing, the higher spatial resolution of voltage pulsing usually results in improved cluster detection [122] and more likely in better crystallographic information [123].

### 7.1.3 Limitations and artefacts

There are limitations and artefacts in APT analysis that need to be understood in order to correctly interpret the results. Artefacts can be related to preferential evaporation of certain atomic species, meaning that species that evaporate at a lower evaporation field than the average evaporation field of the phase in question can evaporate between pulses if the field between pulses is too high. Similarly, preferential retention can occur when the field during pulsing is too low to evaporate species that require a higher-than-average evaporation field. Another artefact related to the difference in evaporation field between species is local magnification, which can occur for phases having a lower or higher evaporation field than the matrix. If the evaporation field of the species in a particle embedded in the matrix is lower than the evaporation field of the matrix, the local magnification is lower, resulting in a smaller reconstructed size and a higher measured atomic concentration of the particle. If the evaporation field of the species of a particle, instead, is higher than the evaporation field of the matrix, the local magnification is higher, resulting in a larger reconstructed size and a lower measured atomic concentration of the particle. Another artefact is related to surface migration of certain species, especially in laser pulse mode. When the specimen is heated by the pulse, some species migrate along the specimen surface and evaporate at a position some distance away from their original position, often at crystallographic poles. Species with a higher evaporation field than the matrix are more likely to surface migrate due to their prolonged time at the specimen surface.

Another limitation of APT analysis is the risk of specimen fracture. Often, the analysis is terminated due to specimen fracture. The probability of fracture is very material dependent and is also affected by the analysis parameters. The stress,  $\sigma$ , in the specimen is proportional to the square of the electric field,  $F$ , according to

$$\sigma = \varepsilon_0 F^2 / 2, \quad (7.4)$$

where  $\varepsilon_0$  is the vacuum permittivity.

Voltage pulsing usually puts more stress on the specimen than laser pulsing, thereby increasing the risk of fracture. Therefore, laser pulsing has to be used for materials that do not withstand the stress imposed by voltage pulsing. These materials include poor electrical conductors and brittle materials. The drawback of using laser pulsing is that the thermally

activated field evaporation usually leads to a slightly decreased spatial resolution compared with voltage pulsing.

Since the mass-to-charge ratio is the chemical information obtained about the evaporated species, the isotopic composition of each element present in the sample has to be used for identification. Usually there are spectral overlaps between some of the species in the sample, precluding certain assignment of spatial position for the individual ions and sometimes limiting the possibilities of accurate identification of elemental composition. Moreover, evaporation and detection of molecular ions, i.e. ions consisting of more than one atom, commonly occur, making mass spectrum evaluation more complicated. Additionally, the peaks in the mass spectrum are not perfectly sharp but have a width. In voltage pulse mode this width is caused by the extension of the pulse in time giving some of the field-evaporated ions energies slightly lower than the maximum energy of the pulse (this is termed energy deficit), and in laser pulse mode it is caused by heating of the specimen, giving so-called thermal tails to the peaks. The extension of the peaks along the mass-to-charge ratio axis often increases peak overlap and complicates mass spectrum evaluation further. The use of a reflectron can compensate the energy deficit in voltage mode, and the thermal effects in laser mode can be minimised by adjustment of analysis parameters. The difference in time between the evaporation events cannot, however, be compensated by the reflectron.

Although APT analysis is sensitive to ions of all mass-to-charge ratios, and accordingly also to all elements of the periodic table, the analysis of H content in the specimen can be difficult due to the presence of residual hydrogen gas in the vacuum chamber. The H atoms can bond to atoms at the specimen surface, forming molecules that evaporate at a lower field than the individual specimen atoms. Therefore, hydride peaks often appear in the mass spectrum, especially for specimens containing elements with high affinity for H. Peaks from H and H<sub>2</sub> also appear in the mass spectrum, meaning that field desorption of some of the H atoms that bond to the specimen surface occurs during the pulses.

A further limitation of APT is the detection efficiency of the instrument. This limitation is usually not of major concern, since the detection efficiency is the same irrespective of mass-to-charge ratio. However, small clusters might not be observed due to all ions not being detected. In modern commercial instruments, the detection efficiency is in the approximate ranges 57 %–80 % and 37 %–50 % for instruments without and with reflectron, respectively. The reason for the lower values for instruments with reflectron is that there are grids in the reflectron that some of the ions hit.

#### 7.1.4 Atom probe tomography of Zr alloys

A number of APT studies of Zr alloys, either in the as-produced state or exposed to various environments prior to analysis, have been performed and published in e.g. [32,33,69,70,84,92,95,124–129], of which [69] is a publication of results from analyses of the same material as in the two appended papers of this thesis. In all these publications referred to, the presented results have been obtained using laser pulsing. When voltage pulse mode is used, unirradiated Zr alloys are prone to fracture [124,126,127,130,131].

Zr has high affinity for H, and Zr hydride species (ZrH and often also ZrH<sub>2</sub>) are usually detected in APT analyses. The detection of Zr hydride species can be due to the existence of dissolved or precipitated H in the specimen that can have been incorporated to the sample during exposure to autoclave corrosion or reactor operation or during sample preparation.

Also the hydrogen gas present in the vacuum system in the atom probe instrument can contribute to the detection of Zr hydride species if it adsorbs on the specimen and is co-evaporated with Zr. Especially the data evaluation of Nb-containing Zr alloys can be complicated by the presence of Zr hydrides and Nb hydrides, since there are spectral overlaps between peaks of these species. Other overlaps that occur in Zr alloys are overlaps between  $\text{Cr}^+$  and  $\text{ZrC}^{2+}$ , between  $\text{Fe}^+$  and  $\text{ZrO}^{2+}$ , and between  $\text{Ni}^+$  and  $\text{Sn}^{2+}$ . To avoid these overlaps a high field is beneficial so that Cr, Fe, and Ni evaporate as  $\text{Cr}^{2+}$ ,  $\text{Fe}^{2+}$ , and  $\text{Ni}^{2+}$  [132]. As the field generally is higher in voltage mode than laser mode, voltage pulsing, if feasible, should be beneficial to overcome these overlaps. However, there are also overlaps between isotopes of Cr and Fe, Fe and Ni, and  $\text{Ni}^{2+}$  and  $\text{Zr}^{3+}$  that need to be accounted for. Figure 7.4 shows two mass spectra from APT analysis of in-BWR-exposed Zircaloy-2, one obtained using voltage pulsing and one obtained using laser pulsing.

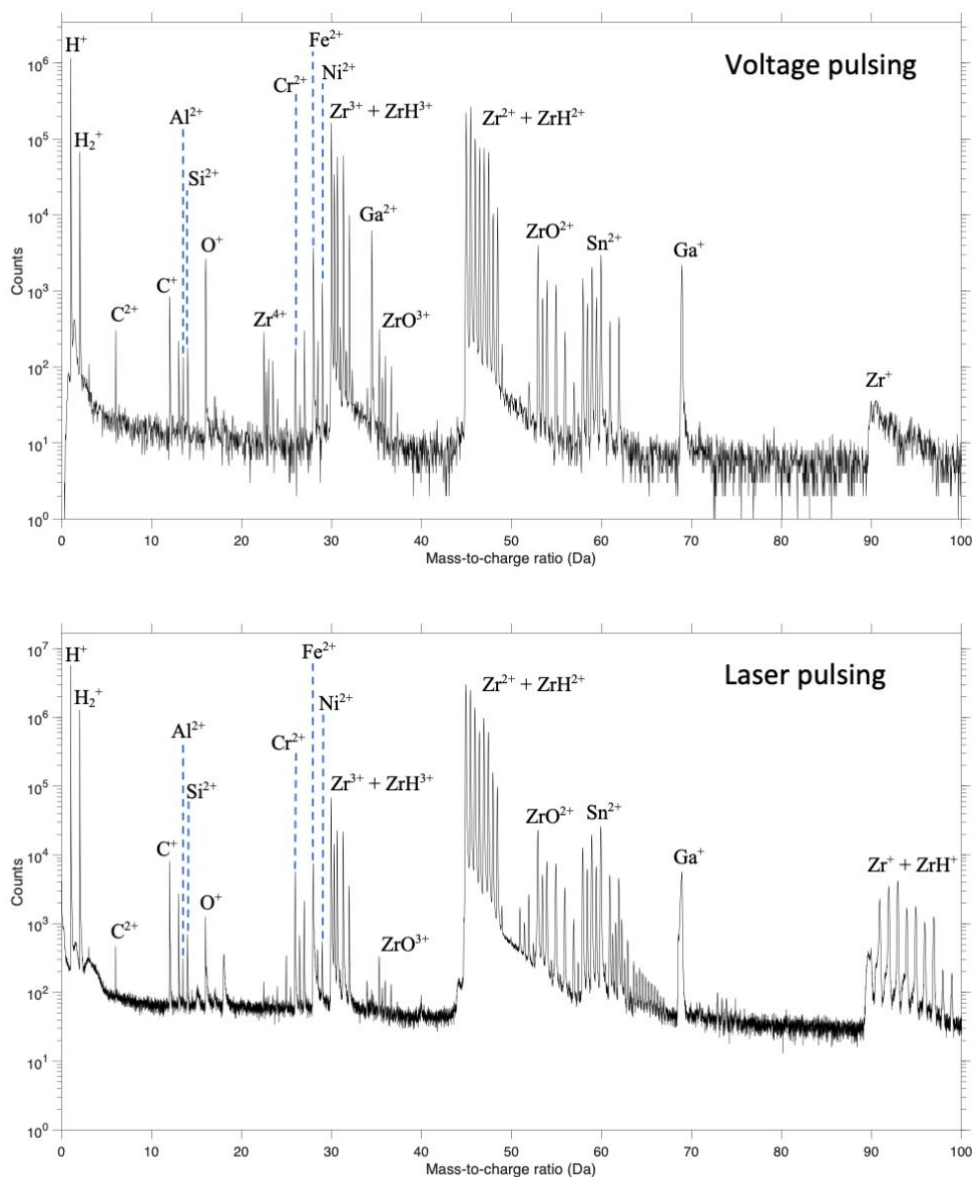


Figure 7.4: Mass spectra of Zircaloy-2 exposed to BWR operation. The majority of the important peaks are labelled. The Ga comes from the sample preparation process using focused ion beam–scanning electron microscopy. Different binning was used for the two histograms.

Because of surface migration of Sn, the Sn distribution in the sample might not always be properly reconstructed, and Sn is often detected at crystallographic poles [95]. However, APT observations of Sn-clustering in the oxide of autoclave-corroded Zircaloy-2 have been made [95].

## 7.2 Sample preparation

The objective of specimen preparation is to create a needle that is sharp enough (radius below 100 nm) to enable field evaporation at a voltage that is lower, preferably much lower, than 15 kV. There are two conventional ways of preparing samples for APT, electropolishing and the lift-out technique using focused ion beam–scanning electron microscopy (FIB–SEM). Electropolishing is the traditional way of preparing APT specimens, and the FIB–SEM lift-out technique has been developed more recently. Which specimen preparation technique that is most suitable to use is material dependent, and it also depends on and the size of the sample and whether the analysis needs to be site specific.

### 7.2.1 Electropolishing

Electropolishing is performed in an electrochemical cell. A rod-shaped piece of the material to be analysed is placed vertically in the cell, which contains one lower region of inert liquid and one upper region of electrolyte. The specimen is connected via cables to a counter electrode that is likewise placed in the cell. When a voltage is applied, electropolishing occurs on the part of the specimen that is covered by the electrolyte. Eventually a neck-shape will form on the specimen. Usually, the electrolyte is replaced by a weaker solution to perform the succeeding part of the electropolishing until the neck of the specimen breaks and two needles are formed. A schematic of an electropolishing setup is shown in Figure 7.5.

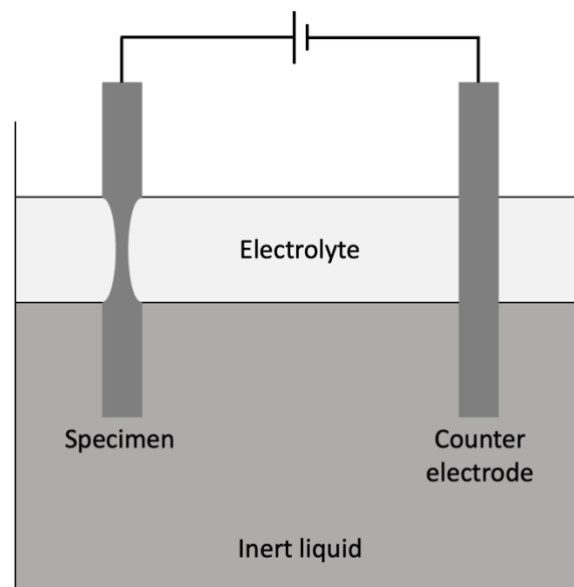


Figure 7.5: Schematic of the electrochemical cell used for electropolishing.

A prerequisite for electropolishing of a material is that it has good enough electrical conductivity. Also, it has to be possible to construct an electrochemical cell using that material. In addition to the material requirements, a limitation of electropolishing is that it is difficult to control the process in such a way that specific features, e.g. grain boundaries, phase boundaries, and SPPs, are incorporated into the outermost part of the final needle. In the case of Zr alloys, electropolishing is possible, although the formation of anodic oxides can be a problem [32,133].

### 7.2.2 Focused ion beam–scanning electron microscopy

FIB–SEM instruments combine a focused ion beam (FIB) with an SEM. In SEMs, samples are studied using electrons that are generated in an electron source and accelerated and focused through a column with electromagnetic lenses before interacting with the sample. The electron beam can be scanned over the sample surface. Depending on what is to be studied, various detectors can be used to collect signals from e.g. back-scattered electrons, secondary electrons, or X-rays. SEMs are usually good tools for imaging conductive materials or non-conductive materials with a conductive coating. FIBs work in a similar way, but the probing particles are ions instead of electrons. The ions can also be used for milling in the sample. Most commonly, liquid metal ions, especially Ga, are used, but in recent years FIBs having plasma ion sources have increased in number.

Usually FIB–SEMs include a system for deposition of material on the sample surface. This is done by introducing the material to be deposited in a precursor gas that adsorbs onto the surface while scanning the ion or electron beam over the surface. The precursor gas then splits up into a volatile compound that leaves the surface and a non-volatile compound that remains at the surface. C, Pt, W, and Au are materials that are common to deposit [134]. With a micromanipulator incorporated in the FIB–SEM it is possible to do lift-outs from the sample. Milling is done around the part to be lifted out before using the gas deposition system to solder the micromanipulator to the part and subsequently using milling to cut the part loose from the rest of the sample. There are various ways of doing lift-outs for APT specimens. One common way is to mill trenches at the two long sides of a rectangular site of interest at an angle of approximately  $30^\circ$  to the surface normal so that a wedge-shaped lift-out (i.e. a lift-out in the form of a triangular prism) is obtained [135]. The lift-out can then be divided into parts that are individually soldered to commercially available Si posts on a wafer containing many posts (e.g.  $6 \times 6$ ). Needles suitable for APT analysis are created by FIB milling of the lifted-out material attached to the Si posts. Figure 7.6 shows the process of FIB–SEM preparation of APT specimens, and Figure 7.7 shows a sharpened tip.

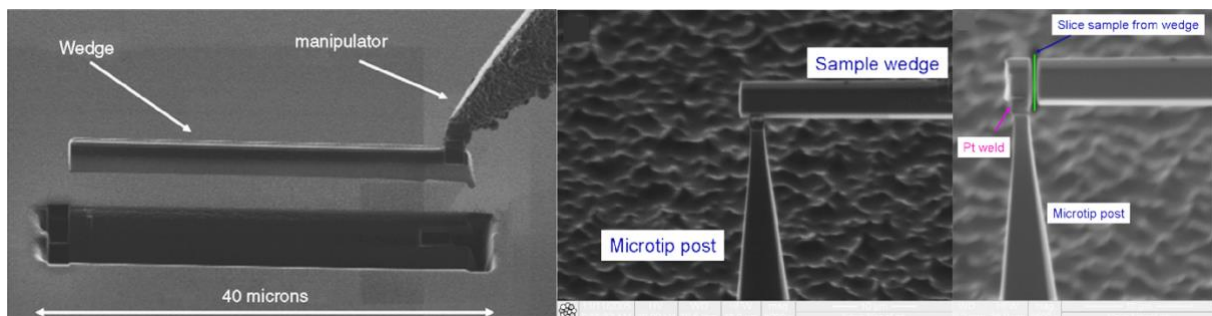
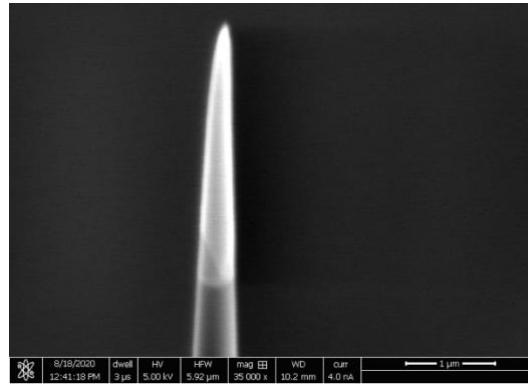


Figure 7.6: FIB–SEM lift-out and attachment of specimen to microtip post. Adapted from [135]. Reprinted with permission from Elsevier.



*Figure 7.7: A sharpened APT specimen.*

An advantage of FIB–SEM preparation is the possibility to do site-specific lift-outs to capture features of interest. It is usually also possible to prepare specimens from materials that are not suitable for electropolishing. An additional advantage is that the sample can be very small (which is preferred for radioactive samples). FIB–SEM operation might, on the other hand, require more training than electropolishing. Also, the equipment needed is more expensive. Most labs having APT instruments, however, usually have FIB–SEMs too.



## 8. Material studied

The material studied in the research of this thesis is presented in this chapter. A brief description of its characteristics compared with the previously utilised material is given, followed by information on the exposure of the samples studied in the two appended papers of this thesis.

Depending on the amount of alloying elements within the given range and the heat treatment process during manufacture, various types of Zircaloy-2 can be produced. The average SPP size, and accordingly also the SPP number density, are determined by the heat treatment of the material. A normalised heat treatment parameter,  $A$ , is used to describe the heat treatment according to

$$A = \sum t_i \exp(-Q/(RT_i)), \quad (8.1)$$

where  $t_i$  is the time of the  $i$ th heat treatment after quenching from the  $\beta$  phase,  $Q$  is the activation energy ( $= 264$  kJ/mol),  $R$  is the ideal gas constant, and  $T_i$  is the absolute temperature of the  $i$ th heat treatment after quenching from the  $\beta$  phase [136].

The size and number density of the SPPs are important for the corrosion and HPU properties of the material in reactor [137]. Two types of Zircaloy-2 that have been and are, respectively, in use in BWRs are the Westinghouse materials LK2 and LK3, where LK is the Swedish acronym for low corrosion (låg korrosion). In addition to small differences in content of alloying elements of the two materials, the heat treatment is different so that a smaller SPP size is obtained in LK2. LK3 was developed as successor to LK2 to mitigate the high corrosion rate and HPU resulting from the small SPP size [93]. When comparing LK2 and LK3, LK3 has a lower uniform corrosion rate, a decreased risk of spacer shadow corrosion, and a delayed onset of accelerated growth [93,138].

The material used in this study (in both Paper I and Paper II) is Zircaloy-2 of the LK3 type of the same lot as studied in [69]. Its heat treatment parameter was  $\log A = -13.9$ , and its nominal composition of alloying elements and main impurities is given in Table 8.1. Prior to analysis, the material was used as cladding tubes in the commercial BWR at Kernkraftwerk Leibstadt (KKL) in Switzerland as part of the Westinghouse fuel performance programme. Fuel rods that have been in operation for three to nine annual cycles (3C–9C) within this programme have been studied and characterised in previous work [34,35,53,61,66,69,71,87–89,139–147]. The samples analysed in the work presented in the two papers of this thesis were exposed for 3C (Paper II) and 9C (Paper I and Paper II). Table 8.2 shows the rod average burnup, specimen elevation, specimen fast neutron fluence exposure, specimen dose, rod average oxide thickness, rod average H content, rod average HPUF, and rod growth of the samples. In the as-produced material, the mean SPP diameter was 84 nm [86] and the SPP number density  $6.4 \times 10^{19} \text{ m}^{-3}$  [66]. After 3C no SPP number density is given in [66], but after 5C and 9C it is given as  $2.2 \times 10^{19} \text{ m}^{-3}$  and  $1.0 \times 10^{19} \text{ m}^{-3}$ , respectively.

Table 8.1: Composition of the Zircaloy-2 of LK3 type studied in the two papers of this thesis. Values from [69].

Element	Concentration
Sn	1.32 (wt%)
Fe	0.17 (wt%)
Cr	0.10 (wt%)
Ni	0.05 (wt%)
O	0.13 (wt%)
Si	70 (wt ppm)
N	50 (wt ppm)

Table 8.2: Burnup, elevation, fast neutron fluence, dose, oxide thickness, H content, HPUF, and growth for the samples studied in the two papers of this thesis.

	3C	9C
Rod average burnup <sup>1</sup> (MWd/kgU)	34.7	78.7
Specimen elevation from rod bottom (mm)	2030–2350	1218–1308
Specimen fast neutron fluence ( $E > 1$ MeV) ( $n\ m^{-2}$ )	$7.4 \times 10^{25}$	$16.5 \times 10^{25}$
Dose <sup>2</sup> (dpa)	11.9	26.5
Rod average oxide thickness <sup>1</sup> ( $\mu\text{m}$ )	$5 \pm 2$	$45 \pm 7$
Rod average H content <sup>1</sup> (wt ppm)	$44 \pm 2$	$664 \pm 94$
HPUF <sup>1</sup> (%)	12.8	30.0
Rod growth <sup>1</sup> (mm)	10.5	28.5

<sup>1</sup>Values from [66].

<sup>2</sup>Calculated from the fast neutron fluence ( $E > 1\text{MeV}$ ) using the conversion factor for BWRs in Table 1 in [47].

## 9. Summary of results and discussion

This chapter summarises the two appended papers of this thesis. Both papers present results that have been obtained by evaluating APT data from experiments performed by Gustav Sundell during his PhD project [148]. The material studied is the Zircaloy-2 of LK3 type described in chapter 8, and the specimens were prepared in the metal close to the metal/oxide interface. The sample preparation was carried out in the hotlab at Studsvik Nuclear AB, where there is a FIB–SEM instrument dedicated for radioactive material.

### 9.1 Summary of Paper I

Paper I presents details on differences between clusters consisting mainly of Fe and Ni and clusters consisting mainly of Fe and Cr in Zircaloy-2 of LK3 type exposed to nine annual cycles of operation in the BWR at KKL. In contrast to previous APT analyses of Zr alloys, the results in this paper were obtained using voltage pulsing and not laser pulsing. The observed Fe–Ni clusters appeared dilute and disc-shaped with a diameter in the range 5–15 nm and a thickness of 2–4 nm. The observed Fe–Cr clusters appeared dense and spheroidal with an approximate diameter of 5 nm. A typical Fe–Ni cluster and a typical Fe–Cr cluster are shown in Figure 9.1. There were small amounts of Ni atoms in the Fe–Cr clusters and very small amounts of Cr atoms, preferentially located close to the cluster edge, in the Fe–Ni clusters. Zr was the main element in both cluster types. The concentrations of Fe and Cr were higher in the Fe–Cr clusters, and the concentration of Ni was approximately equal in both cluster types. Sn was on average not significantly enriched in the clusters, and the Sn concentration varied largely between the clusters. As the crystallographic directions of the reconstruction could be established, it was possible to determine that the clusters were located at expected positions of  $\langle a \rangle$  loops, which were aligned in layers normal to the  $\langle c \rangle$  direction. Fe–Ni clusters occupied planes corresponding to planes that were close to all three families of first-order prismatic planes. As these planes were inclined to the  $\langle c \rangle$  direction, the loops were not located exactly on the prismatic planes. Within each layer of clusters, both Fe–Cr spheroids and Fe–Ni discs were present, with the Fe–Ni discs corresponding to all three families of first-order prismatic planes. The Fe–Ni discs had an enrichment corresponding to about half a monolayer (ML) of an FCC Fe (111) surface, whereas the Fe–Cr spheroids had an enrichment corresponding to about two such MLs. This indicates that the Fe–Ni discs, but probably not the Fe–Cr spheroids, might be segregation inside  $\langle a \rangle$  loops.

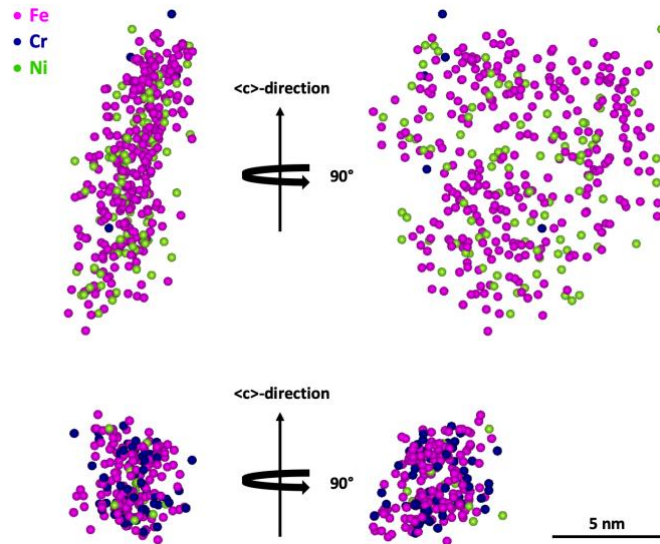


Figure 9.1: A typical Fe–Ni cluster and a typical Fe–Cr cluster. The Fe–Ni cluster is disc-shaped and the Fe–Cr cluster spheroidal. The  $\langle c \rangle$  direction of the matrix is indicated by the arrows.

In the whole analysed volume, both in the clusters and in the matrix surrounding the clusters, Fe was the clustering element that was detected in largest amount, and there was much more Ni than Cr. This type of Ni-rich region has not been observed in previous APT analyses of irradiated Zircaloy-2 [69,70], although these previous studies were performed on a higher number of specimens. As the total alloy content of Cr is higher than that of Ni and as the  $\text{Zr}(\text{Fe,Cr})_2$  SPPs dissolve prior to the  $\text{Zr}_2(\text{Fe,Ni})$  SPPs, it should be more likely to encounter regions rich in Cr than Ni. The combination of the Fe content being higher in the as-produced material and the previous observations of Fe being the first element dissolved from the SPPs [34,35,66] makes it reasonable that more Fe than Cr and Ni was detected in both the clusters and the matrix in the study presented in Paper I and in the previous APT studies [69,70].

The observed chemistry of the two types of clusters resembles the chemistry of the two types of SPPs, where small amounts of Ni have been observed in the  $\text{Zr}(\text{Fe,Cr})_2$  SPPs, but almost no Cr has been observed in the  $\text{Zr}_2(\text{Fe,Ni})$  SPPs [33,35,70].

The observation of disc-shaped clusters was not made in the previous APT studies of in-BWR-exposed Zircaloy-2 [69,70]. In these studies, only spheroidal Fe–Cr clusters were observed. However, segregation of Fe and Ni inside interstitial  $\langle a \rangle$  loops of 10 nm diameter and to the edge of vacancy loops of 10 and 18 nm diameter has been predicted in modelling [149,150]. The observation of disc-shaped Fe–Ni clusters agrees well with the prediction for segregation to interstitial loops. Fe has in another modelling study been predicted to be more likely than Sn, Cr, and Ni to segregate to prismatic stacking faults [46]. This is in line with the observations of the presence of Fe and absence of Sn and Cr, but not with the presence of Ni, at the dilute disc-shaped clusters.

## 9.2 Summary of Paper II

Paper II presents a comparison of Zircaloy-2 of LK3 type exposed to three and to nine annual cycles of operation in the BWR at KKL. Two examples of reconstructions (of 3C specimens) are shown in Figure 9.2. The experimental work was performed using APT in laser mode. In the analysis, a high number density of grain boundaries, most probably subgrain boundaries formed during the growth of oxide, was observed. There was enrichment of especially Sn and Fe, but also small amounts of Cr and very small amounts of Ni, at these grain boundaries. After both 3C and 9C, spheroidal clusters, typically 5 nm in diameter, containing Fe and Cr were observed in most specimens. They were generally aligned in layers in the way  $\langle a \rangle$  loops typically are aligned [49,50,53]. Ni was only in a few grains observed to be located in clusters. Large grain-to-grain variations were observed, but there was on average no difference in cluster number density between the two exposure times, in agreement with a saturation of the number density of  $\langle a \rangle$  loops observed with TEM [53,151]. The number of Fe and Cr atoms per cluster and the ratio Fe/(Fe + Cr) varied largely between individual clusters and between individual grains. However, the clusters were on average larger and more Cr rich after 9C. Large Cr-rich clusters were, in agreement with previous APT observations [70], observed to be preferentially located close to grain boundaries. Sn was observed to be preferentially located between the layers of Fe–Cr clusters, similar to previous TEM observations of Sn being preferentially located between layers of Fe–Ni clusters [53]. Clusters of Sn were observed in regions that had very low concentrations of Fe and Cr. The regions with Sn clusters were adjacent to regions that contained more Fe and Cr and had a higher O content and a slightly lower H content. This is an indication that Sn clusters might form in hydride phases. It is in line with previous observations of the Sn solubility [126] and the overall alloying element content [71,88] being lower in hydride phases. The reason for not observing a larger difference in H content between the regions with and without Sn clusters might be related to the tendency of H to redistribute during cool-down [100] and during sample preparation [113,114].

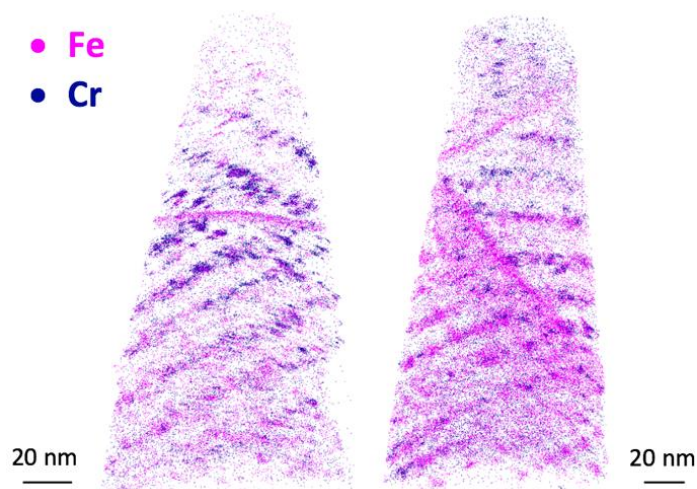


Figure 9.2: Reconstructions of two 3C specimens. Clusters of Fe and Cr are aligned in layers that are perpendicular to the  $\langle c \rangle$  direction of the matrix of each grain.

Ring-shaped features that most likely are <c> component loops were observed in a few of the 9C specimens but in none of the 3C specimens. Sn and Fe were enriched at all these features, and Ni was enriched at one of them. At this latter feature there was much more Fe than Sn, whereas at the other features there was much more Sn than Fe. The size of the observed features was smaller than the size of previously observed <c> component loops [49,53]. Due to the small volume of an APT analysis it is, however, not possible to detect large <c> component loops in their entirety.

In one of the 3C specimens, the observation of a partially dissolved  $Zr(Fe,Cr)_2$  SPP was made. In addition to Fe and Cr, Ni and Si were observed to be located inside the SPP. This observation is in line with previous observations of Ni and Si being present in  $Zr(Fe,Cr)_2$  SPPs [33,35,70]. Hydrogen was observed to be preferentially located in the Zr matrix outside the SPP. Preferential accommodation of H in the Zr matrix surrounding  $Zr(Fe,Cr)_2$  SPPs has been proposed in a study combining nanoscale secondary ion mass spectrometry (NanoSIMS), SEM combined with energy-dispersive X-ray spectroscopy (EDX), and DFT modelling [152]. The observation presented in Paper II thus is in good agreement with that proposed localisation of H.

### 9.3 Discussion

The two papers in this thesis clearly show that the alloying elements behave in different ways under conditions of reactor operation. Partitioning of Ni to one type of cluster and Cr to another type of cluster, as observed in Paper I, might not be surprising considering the partitioning of Ni and Cr to two different types of SPPs. The presence of Ni in the Fe–Cr clusters is analogous to the presence of Ni in  $Zr(Fe,Cr)_2$  SPPs.  $Zr_2(Fe,Ni)$  SPPs have been proposed to be nucleation sites for  $Zr(Fe,Cr)_2$  SPPs [35]. Small Fe–Ni clusters might, similarly, be nucleation sites for Fe–Cr clusters. The slower diffusion of Cr compared with Fe and Ni [39] should lead to Fe–Ni clusters nucleating before Fe–Cr clusters in regions where both Cr and Ni are present. A difference in behaviour between Fe and Cr is evident from the observation in Paper II of Cr-rich clusters being preferentially located close to grain boundaries. In addition to the slower diffusion of Cr, a difference in solubility between Fe and Cr could be part of the explanation of the difference in clustering. The observation of Sn on average not being significantly enriched in the clusters (Paper I) and being preferentially located between the layers of clusters (Paper II) indicates that Sn behaves differently from Fe, Cr, and Ni. This should not be surprising as, Sn, contrary to Fe, Cr, and Ni, in the as-produced material is in solid solution. The different behaviours of the alloying elements might impact the corrosion and HPU properties of the material. Growth and creep might also be affected by the different behaviours of the alloying elements. Modelling might be a good tool in order to understand how corrosion, HPU, growth, and creep are affected by the observations made in the two papers, e.g. the tendency of forming two different cluster types, the preferential location of Cr-rich clusters close to grain boundaries, and Sn being preferentially located between the layers of clusters. As there is no large difference between 3C and 9C regarding Fe–Cr clusters, they might not contribute very much to breakaway growth and breakaway corrosion. As the Fe–Ni clusters were observed only after 9C and as Fe and Ni, but not Cr, were observed at <c> component loops, it is not unlikely that Fe–Ni clusters somehow contribute to breakaway growth and breakaway corrosion.

The hydrogen content in the analyses presented in both papers was high (20–60 at.%). As mentioned in both Paper I and Paper II, it is not possible to determine when the hydrogen was incorporated into the specimen volumes. H might have been introduced in the part of the

material corresponding to the specimen volumes during reactor operation, during cool-down, or during sample or specimen preparation, and it might (at least partly) emanate from the residual gas in the vacuum system of the APT instrument. A combination of two or more of these routes of H introduction is also possible. As the distribution of H and hydrides is not the same during reactor operation as post service, it is generally difficult to know whether observed hydrides were hydrides also during reactor operation. However, as there is (almost) no neutron flux and lower temperature post service compared with operation, the alloying elements should not be redistributed post service. As long as no other artefacts are induced during sample or specimen preparation, it can thus be assumed that the observed chemical features (excluding H) are representative of the material during reactor operation. To reduce the hydrogen implantation during specimen preparation, a cryo FIB could be used, but it would not necessarily give more information about the hydrogen distribution during reactor operation.

The fact that the use of voltage-pulsed APT on BWR-exposed Zircaloy-2 was successful indicates that the irradiation has strengthened the material enough to sustain the higher stress of voltage pulsing compared with laser pulsing. Two out of a total of four attempted runs were successful. Although this is not a very high success rate, it indicates that voltage pulsing probably is a viable method for future APT studies of irradiated Zr alloys.



## 10. Future work

In order to better understand how the results of the research presented in this thesis affect the processes that degrade Zr alloys in nuclear reactors, more studies need to be undertaken. Suggestions for future work are given in this chapter.

The observations made in this thesis could be put into a wider context if more examinations of irradiated Zircaloy-2 were performed. More studies of Ni-rich regions might confirm the difference in cluster shape between Fe–Cr and Fe–Ni clusters. Using TEM or TKD in correlation with APT might allow for a more thorough investigation of the crystallography of the irradiated microstructure. Furthermore, it would be interesting to know if the clusters are located at either or both of interstitial and vacancy loops. As this determination can be difficult using experimental techniques, e.g. TEM (because of the small loop size) [53], modelling might be necessary to predict the preferred segregation of the alloying elements to small loops.

It would be of interest to gain a better understanding of the reason for the large variations between individual grains and regions within the samples. Although more APT analyses might give additional information about these differences, the very small volume of an APT analysis makes it unlikely that APT alone will yield sufficient information. More TEM and scanning TEM (STEM) analyses combined with EDX could give more information about elemental distributions on a larger scale, resulting in a better overview of differences between different regions. Using these techniques it might be possible to perform detailed studies of regions of interest, such as SPPs and hydrides. However, as a large number of studies using various techniques already have been performed, additional information might also be obtained by reviewing these studies.

As a higher Fe content has shown to decrease HPU [18], it is of interest to study the difference between Zircaloy-2 and alloys with higher Fe content. At present, there are samples of a model alloy called Alloy 2 at Chalmers University of Technology. This alloy has higher Fe and higher Cr content than Zircaloy-2 and is similar to the recently developed commercial alloy HiFi (which has a lower Cr content than Alloy 2). Samples that have been exposed to autoclave corrosion and to reactor operation are available, as well as unexposed reference material. There is in-reactor-exposed material from both the fuel region and the plenum region of the core. Also Zircaloy-2 of LK3 type with the same exposure is available. APT and TEM investigations of the metal and the oxide of these materials are planned to be undertaken in an attempt to understand how increased Fe and Cr contents affect the chemical evolution of the material and how this affects the corrosion and HPU properties. It is also intended to study regions in the metal further away from the metal/oxide interface to see how the formation of subgrains affects the microstructural and chemical evolution of the materials. Furthermore, the two different positions of the in-reactor-exposed samples allow for an investigation of how the results are influenced by neutron fluence. Additionally, the liner of each sample can be studied to investigate the effect of a very low content of alloying elements.

To better understand the chemical evolution of the materials, a study of the matrix composition (i.e. the composition excluding SPPs and grain boundaries) of the as-produced materials would be beneficial. The results of such a study could then be compared with the matrix composition of irradiated material, both including and excluding the clusters of alloying elements. It might also be interesting to study how the matrix composition varies

along the radial direction of the cladding tubes. The combination of the high spatial resolution and the high mass resolution of APT makes this technique suitable for measuring the matrix composition. The results of such analyses might be used in modelling aimed at relating the evolution of matrix chemistry to the corrosion and hydrogen pickup of the materials. In addition to the matrix chemistry evolution, it might also be interesting to investigate how the absolute and relative sizes and number densities of  $Zr(Fe,Cr)_2$  and  $Zr_2(Fe,Ni)$  SPPs differ between Zircaloy-2 and Alloy 2 and how they are affected by BWR exposure. The SPP evolution is, of course, related to the matrix chemistry evolution. (S)TEM-EDX is a suitable technique for this type of analysis.

In addition to studying Zircaloy-2 and Alloy 2, it could be of interest to study Zircaloy-4 after in-reactor exposure. As the main difference between Zircaloy-2 and Zircaloy-4 is the absence of Ni in Zircaloy-4, a comparison of these two materials could give more information on the role of Ni in the processes leading to degradation of the cladding.

## Acknowledgements

I would like to thank a number of people who have made me enjoy my time as a PhD student so far:

First of all I would like to thank my main supervisor Mattias Thuvander for giving me the opportunity to do this research and for the excellent support and guidance in this project. Thanks for teaching me atom probe analysis, for discussing interpretation of results, and for giving me constructive feedback on my presentations and drafts, no matter how close to the deadline I send them to you.

Many thanks to my co-supervisor Hans-Olof Andrén. Thank you for your enthusiasm about the subject, sharing your knowledge, and the valuable suggestions for improvement of my drafts.

I would also like to thank my co-supervisor Mohammad Sattari for giving me guidance regarding microscopy. I am looking forward to further collaboration during the continuation of this project.

I am thankful to my industrial collaborators for interesting and valuable discussions, and for providing relevant materials for the continuation of this project. Thank you Magnus Limbäck, Jonathan Wright, Antoine Claisse, and Clara Anghel at Westinghouse, Karin Carling, David Schrire, and Bertil Josefsson at Vattenfall, Reidar Löfström, Henrik Eisenberg, and Marcus Nilsson at OKG.

The members of the MUZIC-3 consortium are acknowledged for fruitful discussions during the many meetings and webinars. Thanks to these meetings my knowledge of zirconium alloys and their degradation has increased a lot.

I would like to thank Mattias Alm at Sandvik AB for showing me the cladding tube production, and I would like to thank Conny Lampa at Höganäs AB for showing me the laser welding facilities and possible applications for zirconium alloys.

Göran Embring, Lars-Eric Bjerke, and Tell Andersson at Onsala Ingenjörbyrå are acknowledged for interesting discussions on nuclear power, zirconium alloys, and accident tolerant fuel. Hopefully, we will get interesting results from our studies of coated cladding tubes. Special thanks to Lars-Eric for teaching me how to play tennis.

Thanks to all my colleagues at the Division of Microstructure Physics, Eva Olsson Group, and Chalmers Materials Analysis Laboratory for company during lunch and coffee breaks. Special thanks to Stefan Gustafsson for assistance with the microscopes and to Ola Löfgren for assistance with computer-related issues. A special thank also to my office mates Kristina and Emil for keeping me company during the many hours spent in the office.

At last, but not least, thanks to my parents Gunnar and Annelie, to my sister Anna, and to my brother Mattias. Thank you for all your love and support!



## References

- [1] IAEA Director General's Introductory Statement to the Board of Governors, 1 March, 2021. <https://www.iaea.org/iaea-director-generals-introductory-statement-to-the-board-of-governors-1-March-2021>. Retrieved 2 March, 2021.
- [2] IPCC, Climate Change 2014: Mitigation of Climate Change. Working Group III Contribution to the Fifth Assessment Report of the Intergovernmental Panel on Climate Change, Cambridge University Press, 2014.
- [3] L. Gagnon, C. Bélanger, Y. Uchiyama, *Energy Policy* 30 (2002) 1267–1278.
- [4] A. Markandya, P. Wilkinson, *Lancet* 370 (2007) 979–990.
- [5] R.B. Adamson, C.E. Coleman, M. Griffiths, *J. Nucl. Mater.* 521 (2019) 167–244.
- [6] B. Cheng, R. Adamson, *ASTM STP 939 (1987)* 387–416.
- [7] W.E. Berry, D.A. Vaughan, E.L. White, *Corrosion* 17 (1961) 109t–117t.
- [8] G. Choppin, J.-O. Liljenzin, J. Rydberg, *Radiochemistry and Nuclear Chemistry*, 3rd ed., Butterworth-Heinemann, 2002.
- [9] IAEA, *Nuclear Power Reactors in the World*, Reference Data Series No.2, 2017 Edition, IAEA, 2017.
- [10] D.D. Baron, L. Hallstadius, *Fuel Performance of Light Water Reactors (Uranium Oxide and MOX)*, in *Comprehensive Nuclear Materials – Basic Aspects of Radiation Effects in Solid/Basic Aspects of Multi-Scale Modeling*. Editor-in-Chief: R.J.M. Konings, Section Editors: T.R. Allen, R.E. Stoller, S. Yamanaka, Elsevier, 2012.
- [11] C. Lemaignan, A.T. Motta, *Zirconium Alloys in Nuclear Applications*, in *Materials Science and Technology – A Comprehensive Treatment*, R.W. Cahn, P. Haasen, E.J. Kramer (Eds.), Volume 10B: *Nuclear Materials Part II (Chapter 7)*, Volume Editor B.T. Frost, VCH, 1994.
- [12] G. Pfenning, H. Klewe-Nebenuis, W. Seelmann-Eggebert, *Karlsruher Nuklidkarte*, 6th ed., Forschungszentrum Karlsruhe GmbH, 1998.
- [13] Vattenfall. *Tekniska data Ringhals*. <https://group.vattenfall.com/se/siteassets/sverige/ringhals/produktion/tekniska-data-utforlig-ringhals-151207.pdf>. Retrieved 14 August, 2020.
- [14] U.S.NRC. <https://www.nrc.gov/reading-rm/basic-ref/students/animated-pwr.html>. Retrieved 20 March, 2021.
- [15] U.S.NRC. <https://www.nrc.gov/reading-rm/basic-ref/students/animated-bwr.html>. Retrieved 20 March, 2021.
- [16] L. Hallstadius, S. Johnson, E. Lahoda, *Prog. Nucl. Energy* 57 (2012) 71–76.
- [17] H.G. Rickover, in *Zirconium Production and Technology: The Kroll Medal Papers 1975–2010*, pp. 9–17, editor R.B. Adamson, ASTM, 2010.
- [18] Z. Karoutas, J. Brown, A. Atwood, L. Hallstadius, E. Lahoda, S. Ray, J. Bradfute, *Prog. Nucl. Energy* 102 (2018) 68–78.
- [19] ASTM Standard B350/B350M - 11(2016)E1
- [20] A.V. Nikulina, *Met. Sci. Heat Treat.* 45 (2003) 287–292.
- [21] A. Fazi, H. Aboufadi, A.H.S. Iyer, M. Sattari, K.M. Stiller, P. Lokhande, M. Thuvander, H.-O. Andrén, *J. Nucl. Mater.* 549 (2021).
- [22] A.V. Nikulina, *Met. Sci. Heat Treat.* 46 (2004) 458–462.
- [23] A. Jostsons, J.G. Napier, *Crystallographic Techniques and Data for Transmission Electron Microscopy of Zirconium*, Australian Atomic Energy Commission, 1970.
- [24] R.A. Johnson, J.R. Beeler, in: *Proceedings of Interatomic Potentials and Crystalline Defects*, AIME, Pittsburgh, PA, 1981, pp. 165–177.
- [25] G. Vérité, C. Domain, C.C. Fu, P. Gasca, A. Legris, F. Willaime, *Phys. Rev. B* 87 (2013) 134108.
- [26] P.J. Hazell, G.J. Appleby-Thomas, E. Wielewski, J.P. Escobedo, *Philos. Trans. R. Soc. A Math. Phys. Eng. Sci.* 372 (2014) 20130204.
- [27] D.J. Bacon, *J. Nucl. Mater.* 206 (1993) 249–265.
- [28] A.R. Verma, O.N. Srivastava, *Crystallography for Solid State Physics*, Wiley Eastern Limited, 1982.
- [29] D. Hull, D.J. Bacon, *Introduction to Dislocations*, 5th ed., Butterworth-Heinemann, 2011.
- [30] V.G. Kapinos, Y.N. Osetsky, P.A. Platonov, *J. Nucl. Mater.* 195 (1992) 83–101.
- [31] D.E. Laughlin, B.Y. Wong, *IEEE Trans. Magn.* 27 (1991) 4713–4717.
- [32] M. Thuvander, H.-O. Andrén, *Ultramicroscopy* 111 (2011) 711–714.
- [33] T. Sawabe, T. Sonoda, S. Kitajima, T. Kameyama, *J. Nucl. Mater.* 442 (2013) 168–174.

- [34] S. Abolhassani, D. Gavillet, F. Groeschel, P. Jourdain, H.U. Zwicky, in: Proceedings of International Topical Meeting LWR Fuel Performance, April 10–13, Park City, Utah, USA, 2000, pp. 470–484.
- [35] A. Harte, M. Topping, P. Frankel, D. Jädernäs, J. Romero, L. Hallstadius, E.C. Darby, M. Preuss, *J. Nucl. Mater.* 487 (2017) 30–42.
- [36] P. Rudling, K. Lundblad Vannesjö, G. Vesterlund, A.R. Massih, *ASTM STP 939* (1987) 292–306.
- [37] Y. Ito, T. Furuya, *J. Nucl. Sci. Technol.* 32 (1995) 1118–1126.
- [38] Z.D. Shah, *Characterizing and Modelling Precipitation in Zirconium Alloys*, Ph.D. Thesis, University of Manchester, 2019.
- [39] G.M. Hood, *J. Nucl. Mater.* 159 (1988) 149–175.
- [40] E. Tenckhoff, *ASTM STP 1467* (2005) 25–50.
- [41] F. Onimus, J.L. Béchade, *Radiation Effects in Zirconium Alloys*, Elsevier, 2012.
- [42] K. Nordlund, S.J. Zinkle, A.E. Sand, F. Granberg, R.S. Averbach, R.E. Stoller, T. Suzudo, L. Malerba, F. Banhart, W.J. Weber, F. Willaime, S.L. Dudarev, D. Simeone, *J. Nucl. Mater.* 512 (2018) 450–479.
- [43] C.H. Woo, *J. Nucl. Mater.* 159 (1988) 237–256.
- [44] Y.N. Osetsky, D.J. Bacon, N. de Diego, *Metall. Mater. Trans. A Phys. Metall. Mater. Sci.* 33 (2002) 777–782.
- [45] G.D. Samolyuk, A.V. Barashev, S.I. Golubov, Y.N. Osetsky, R.E. Stoller, *Acta Mater.* 78 (2014) 173–180.
- [46] J.F. March-Rico, G. Huang, B.D. Wirth, *J. Nucl. Mater.* 540 (2020) 152339.
- [47] L. Walters, S.R. Douglas, M. Griffiths, *ASTM STP 1597* (2018) 676–690.
- [48] C. Varvenne, O. Mackain, E. Clouet, *Acta Mater.* 78 (2014) 65–77.
- [49] M. Griffiths, *J. Nucl. Mater.* 159 (1988) 190–218.
- [50] A. Jostsons, P.M. Kelly, R.G. Blake, *J. Nucl. Mater.* 66 (1977) 236–256.
- [51] P.M. Kelly, R.G. Blake, *Philos. Mag.* 28 (1973) 415–426.
- [52] D.O. Northwood, R.W. Gilbert, L.E. Bahen, P.M. Kelly, R.G. Blake, A. Jostsons, P.K. Madden, D. Faulkner, W. Bell, R.B. Adamson, *J. Nucl. Mater.* 79 (1979) 379–394.
- [53] A. Harte, D. Jädernäs, M. Topping, P. Frankel, C.P. Race, J. Romero, L. Hallstadius, E.C. Darby, M. Preuss, *Acta Mater.* 130 (2017) 69–82.
- [54] D.O. Northwood, R.W. Gilbert, *J. Nucl. Mater.* 51 (1974) 271–276.
- [55] A. Jostsons, R.G. Blake, J.G. Napier, P.M. Kelly, K. Farrell, *J. Nucl. Mater.* 68 (1977) 267–276.
- [56] C. Dai, L. Balogh, Z. Yao, M.R. Daymond, *J. Nucl. Mater.* 478 (2016) 125–134.
- [57] C. Dai, P. Saidi, M. Topping, L.K. Béland, Z. Yao, M.R. Daymond, *Scr. Mater.* 172 (2019) 72–76.
- [58] B. Christiaen, C. Domain, L. Thuinet, A. Ambard, A. Legris, *Acta Mater.* 179 (2019) 93–106.
- [59] R.A. Holt, R.W. Gilbert, *J. Nucl. Mater.* 137 (1986) 185–189.
- [60] S. Yagnik, R.B. Adamson, G. Kobylansky, J.H. Chen, D. Gilbon, S. Ishimoto, T. Fukuda, L. Hallstadius, A. Obukhov, S. Mahmood, *ASTM STP 1597* (2018) 748–795.
- [61] M. Topping, A. Harte, P. Frankel, C. Race, G. Sundell, M. Thuvander, H.-O. Andrén, D. Jädernäs, P. Tejländ, J.E. Romero, E.C. Darby, S. Dumbill, L. Hallstadius, M. Preuss, *ASTM STP 1597* (2018) 796–822.
- [62] Y. Li, N. Ghoniem, *J. Nucl. Mater.* 540 (2020) 152312.
- [63] B. Christiaen, C. Domain, L. Thuinet, A. Ambard, A. Legris, *Acta Mater.* 195 (2020) 631–644.
- [64] D.G. Franklin, R.B. Adamson, *J. Nucl. Mater.* 159 (1988) 12–21.
- [65] M. Griffiths, R.W. Gilbert, G.J.C. Carpenter, *J. Nucl. Mater.* 150 (1987) 53–66.
- [66] S. Valizadeh, G. Ledergerber, S. Abolhassani, D. Jädernäs, M. Dahlbäck, E.V. Mader, G. Zhou, J. Wright, L. Hallstadius, *ASTM STP 1529* (2011) 729–753.
- [67] P.Y. Huang, S.T. Mahmood, R.B. Adamson, *ASTM STP 1295* (1996) 726–757.
- [68] Y. Etoh, S. Shimada, *J. Nucl. Mater.* 200 (1993) 59–69.
- [69] G. Sundell, M. Thuvander, P. Tejländ, M. Dahlbäck, L. Hallstadius, H.-O. Andrén, *J. Nucl. Mater.* 454 (2014) 178–185.
- [70] T. Sawabe, T. Sonoda, *J. Nucl. Sci. Technol.* 55 (2018) 1110–1118.
- [71] A. Baris, S. Abolhassani, R. Grabherr, R. Restani, R. Schäublin, Y.L. Chiu, H.E. Evans, K. Ammon, M. Limbäck, in: Proceedings of TopFuel, Prague, Czech Republic, 30 September–04 October, 2018, paper A 0172, ENS.
- [72] B.V. Cockeram, P.D. Edmondson, K.J. Leonard, B.F. Kammenzind, J.L. Hollenbeck, *Nucl. Mater. Energy* 19 (2019) 416–432.
- [73] B. Cox, *J. Nucl. Mater.* 172 (1990) 249–292.
- [74] M. Dahlbäck, L. Hallstadius, M. Limbäck, G. Vesterlund, T. Andersson, P. Witt, J. Izquierdo, B. Remartinez, M. Díaz, J.L. Sacedon, A.M. Alvarez, U. Engman, R. Jakobsson, A.R. Massih, M. Billone, M. Elmoselhi, N. Yamashita, B. Cheng, *ASTM STP 1467* (2005) 873–895.

- [75] P. Rudling, Zr Alloy Corrosion and Hydrogen Pickup, ANT International, 2013.
- [76] R. Stevens, An Introduction to Zirconia, 2nd ed., Magnesium Elektron, 1986.
- [77] J. Godlewski, J. Gros, M. Lambertin, J. Wadier, H. Weidinger, ASTM STP 1132 (1991) 416–436.
- [78] B. Cox, J. Nucl. Mater. 336 (2005) 331–368.
- [79] P. Tejlund, C. Langhammer, H.-O. Andrén, J. Nucl. Mater. 400 (2010) 79–83.
- [80] V. Bouineau, A. Ambard, G. Bénier, D. Pêcheur, J. Godlewski, L. Fayette, T. Duverneix, ASTM STP 1505 (2009) 405–429.
- [81] E. Hillner, D.G. Franklin, J.D. Smee, J. Nucl. Mater. 278 (2000) 334–345.
- [82] D. Hudson, N. Ni, S. Lozano-Perez, D. Saxey, C. English, G.D.W. Smith, J. Sykes, C. Grovenor, in: Proceedings of 14th International Conf. Environmental Degradation of Materials in Nuclear Power Systems, Virginia Beach, VA, August 23–27, 2009, ANS.
- [83] P. Tejlund, M. Thuvander, H.-O. Andrén, S. Ciurea, T. Andersson, M. Dahlbäck, L. Hallstadius, ASTM STP 1529 (2011) 595–619.
- [84] Y. Dong, A.T. Motta, E.A. Marquis, J. Nucl. Mater. 442 (2013) 270–281.
- [85] P. Tejlund, H.-O. Andrén, J. Nucl. Mater. 430 (2012) 64–71.
- [86] P. Tejlund, H.-O. Andrén, J. Nucl. Mater. 444 (2014) 30–34.
- [87] A. Garner, F. Baxter, P. Frankel, M. Topping, A. Harte, T. Slater, P. Tejlund, J.E. Romero, E.C. Darby, A. Cole-Baker, M. Gass, M. Preuss, ASTM STP 1597 (2018) 491–523.
- [88] A. Baris, R. Restani, R. Grabherr, Y.L. Chiu, H.E. Evans, K. Ammon, M. Limbäck, S. Abolhassani, J. Nucl. Mater. 504 (2018) 144–160.
- [89] A. Baris, S. Abolhassani, Y.L. Chiu, H.E. Evans, Mater. High Temp. 35 (2018) 14–21.
- [90] Swiss Federal Nuclear Safety Inspectorate (ENSI). Increased local corrosion of SVEA-96 fuel assemblies in KKL Final report (HSK--12/744), 2001.
- [91] D. Pêcheur, F. Lefebvre, A.T. Motta, C. Lemaignan, J.F. Wadier, J. Nucl. Mater. 189 (1992) 318–332.
- [92] G. Sundell, M. Thuvander, H.-O. Andrén, Corros. Sci. 65 (2012) 10–12.
- [93] J. Romero, L. Hallstadius, M. Owaki, G. Pan, K. Kataoka, K. Kakiuchi, R.J. Comstock, J. Partezana, A. Mueller, M. Dahlbäck, A. Garde, A. Atwood, M. Åslund, in: Proceedings of WRFPM/TopFuel, Sendai, Japan, Sept. 14–17, 2014.
- [94] M. Preuss, P. Frankel, S. Lozano-Perez, D. Hudson, E. Polatidis, N. Ni, J. Wei, C. English, S. Storer, K.B. Chong, M. Fitzpatrick, P. Wang, J. Smith, C. Grovenor, G. Smith, J. Sykes, B. Cottis, S. Lyon, L. Hallstadius, B. Comstock, A. Ambard, M. Blat-Yrieix, ASTM STP 1529 (2011) 649–681.
- [95] G. Sundell, M. Thuvander, H.-O. Andrén, J. Nucl. Mater. 456 (2015) 409–414.
- [96] P. Bossis, D. Pêcheur, K. Hanift, J. Thomazet, M. Blat, S. Yagnik, K.Y. Suk, ASTM STP 1467 (2005) 494–525.
- [97] M. Lindgren, G. Sundell, I. Panas, L. Hallstadius, M. Thuvander, H.-O. Andrén, ASTM STP 1543 (2015) 515–539.
- [98] G.P. Sabol, G. Kilp, M. Balfour, E. Roberts, ASTM STP 1023 (1989) 227–244.
- [99] M. Christensen, W. Wolf, C. Freeman, E. Wimmer, R.B. Adamson, L. Hallstadius, P.E. Cantonwine, E.V. Mader, J. Phys. Condens. Matter 27 (2015) 025402.
- [100] J. Bair, M. Asle Zaeem, M. Tonks, J. Nucl. Mater. 466 (2015) 12–20.
- [101] K. Une, S. Ishimoto, Y. Etoh, K. Ito, K. Ogata, T. Baba, K. Kamimura, Y. Kobayashi, J. Nucl. Mater. 389 (2009) 127–136.
- [102] A. McMinn, E.C. Darby, J.S. Schofield, ASTM STP 1354 (2000) 173–195.
- [103] P. Vizcaíno, A.D. Banchik, J.P. Abriata, J. Nucl. Mater. 304 (2002) 96–106.
- [104] M. Christensen, W. Wolf, C.M. Freeman, E. Wimmer, R.B. Adamson, L. Hallstadius, P.E. Cantonwine, E.V. Mader, J. Nucl. Mater. 445 (2014) 241–250.
- [105] J. Blomqvist, J. Olofsson, A.M. Alvarez, C. Bjerkén, in Proceedings of the 15th Int. Conf. on Environmental Degradation of Materials in Nuclear Power Systems—Water Reactors, August 7–11 2011, Colorado Springs, Colorado, USA, editors: J.T. Busby, G. Ilevbare, P.L. Andresen, Springer, 2016, pp. 671–681.
- [106] J. Zheng, X. Zhou, L. Mao, H. Zhang, J. Liang, L. Sheng, S. Peng, Int. J. Hydrogen Energy 40 (2015) 4597–4604.
- [107] Z. Zhao, M. Blat-Yrieix, J.P. Morniroli, A. Legris, L. Thuinet, Y. Kihn, A. Ambard, L. Legras, ASTM STP 1505 (2009) 29–50.
- [108] E. Zuzek, J.P. Abriata, A. San-Martin, F.D. Manchester, Bull. Alloy Phase Diagrams 11 (1990) 385–395.
- [109] J. Goldak, L.T. Lloyd, C.S. Barrett, Phys. Rev. 144 (1966) 478–484.
- [110] S.S. Sidhu, N.S. Satya Murthy, F.P. Campos, D.D. Zaubers, Adv. Chemistry 39 (1963) 87–98.

- [111] S. Yamanaka, K. Yamada, K. Kurosaki, M. Uno, K. Takeda, H. Anada, T. Matsuda, S. Kobayashi, *J. Alloys Compd.* 330–332 (2002) 99–104.
- [112] K. Niedźwiedź, B. Nowak, O.J. Zogał, *J. Alloys Compd.* 194 (1993) 47–51.
- [113] H.H. Shen, X.T. Zu, B. Chen, C.Q. Huang, K. Sun, *J. Alloys Compd.* 659 (2016) 23–30.
- [114] S.M. Hanlon, S.Y. Persaud, F. Long, A. Korinek, M.R. Daymond, *J. Nucl. Mater.* 515 (2019) 122–134.
- [115] B. Gault, M.P. Moody, J.M. Cairney, S.P. Ringer, *Atom Probe Microscopy*, Springer, 2012.
- [116] D.J. Larson, T.J. Prosa, R.M. Ulfing, B.P. Geiser, T.F. Kelly, *Local Electrode Atom Probe Tomography*, Springer, 2013.
- [117] M.K. Miller, R.G. Forbes, *Atom-Probe Tomography: The Local Electrode Atom Probe*, Springer, 2014.
- [118] P. Bas, A. Bostel, B. Deconihout, D. Blavette, *Appl. Surf. Sci.* 87–88 (1995) 298–304.
- [119] J.M. Hyde, C.A. English, *Mater. Res. Soc. Symp. - Proc.* 650 (2001) R6.6.1–R6.6.12.
- [120] D. Vaumousse, A. Cerezo, P.J. Warren, *Ultramicroscopy* 95 (2003) 215–221.
- [121] O.C. Hellman, J.A. Vandenbroucke, J. Rüsing, D. Isheim, D.N. Seidman, *Microsc. Microanal.* 6 (2000) 437–444.
- [122] K. Lindgren, K. Stiller, P. Efsing, M. Thuvander, *Microsc. Microanal.* 23 (2017) 376–384.
- [123] A. Shariq, S. Mutas, K. Wedderhoff, C. Klein, H. Hortenbach, S. Teichert, P. Kücher, S.S.A. Gerstl, *Ultramicroscopy* 109 (2009) 472–479.
- [124] B.V. Cockeram, K.J. Leonard, L.L. Snead, M.K. Miller, *J. Nucl. Mater.* 433 (2013) 460–478.
- [125] A. Harte, R.P. Babu, C.A. Hirst, T.L. Martin, P.A.J. Bagot, M.P. Moody, P. Frankel, J. Romero, L. Hallstadius, E.C. Darby, M. Preuss, *J. Nucl. Mater.* 510 (2018) 460–471.
- [126] A.J. Breen, I. Mouton, W. Lu, S. Wang, A. Szczepaniak, P. Kontis, L.T. Stephenson, Y. Chang, A.K. da Silva, C.H. Liebscher, D. Raabe, T.B. Britton, M. Herbig, B. Gault, *Scr. Mater.* 156 (2018) 42–46.
- [127] I. Mouton, A.J. Breen, S. Wang, Y. Chang, A. Szczepaniak, P. Kontis, L.T. Stephenson, D. Raabe, M. Herbig, T.B. Britton, B. Gault, *Microsc. Microanal.* 25 (2019) 481–488.
- [128] Z. Yu, T. Kim, M. Bachhav, X. Liu, L. He, A. Couet, *Corros. Sci.* 173 (2020) 108790.
- [129] E.J. Kautz, B. Gwalani, S.V.M. Lambeets, L. Kovarik, D.K. Schreiber, D.E. Perea, D. Senor, Y.-S. Liu, A.K. Battu, K.-P. Tseng, S. Thevuthasan, A. Devaraj, *NPJ Mater. Degrad.* 4 (2020) 29.
- [130] B. Wadman, H.-O. Andrén, U. Rolander, *Le J. Phys. Colloq.* 49 (1988) C6-323–C6-327.
- [131] B. Wadman, H.-O. Andrén, A.L. Nyström, P. Rudling, H. Pettersson, *J. Nucl. Mater.* 200 (1993) 207–217.
- [132] D.R. Kingham, *Surf. Sci.* 116 (1982) 273–301.
- [133] H.-O. Andrén, L. Mattsson, U. Rolander, *Le J. Phys. Colloq.* 47 (1986) C2-191–C2-196.
- [134] J. Orloff, M. Utlaut, L. Swanson, *High Resolution Focused Ion Beams: FIB and Its Applications*, Springer, 2003.
- [135] K. Thompson, D. Lawrence, D.J. Larson, J.D. Olson, T.F. Kelly, B. Gorman, *Ultramicroscopy* 107 (2007) 131–139.
- [136] T. Andersson, T. Thorvaldsson, A. Wilson, A.M. Wardle, in: *Improvements in Water Reactor Fuel Technology and Utilization*. IAEA-SM-288/59, Vienna, Austria, 1987, pp. 435–449, IAEA.
- [137] P. Tägtström, M. Limbäck, M. Dahlbäck, T. Andersson, H. Pettersson, *ASTM STP 1423* (2002) 96–118.
- [138] G. Ledergerber, W. Kaufmann, A. Ritter, D. Greiner, Y. Parmar, R. Jacot-Guillarmod, J. Krouthén, in: *Proceedings of the International LWR Fuel Performance Meeting, San Francisco, California, USA, Sept. 30 – Oct. 3 (2007) Paper 1036*.
- [139] G. Ledergerber, S. Abolhassani, M. Limbäck, R.J. Lundmark, K.-Å. Magnusson, *J. Nucl. Sci. Technol.* 43 (2006) 1006–1014.
- [140] G. Kuri, C. Degueudre, J. Bertsch, S. Abolhassani, *Appl. Phys. A Mater. Sci. Process.* 98 (2010) 625–633.
- [141] G. Ledergerber, S. Valizadeh, J. Wright, M. Limbäck, L. Hallstadius, D. Gavillet, S. Abolhassani, F. Nagase, T. Sugiyama, W. Wiesenack, T. Tverberg, in: *Proceedings of LWR Fuel Performance Meeting/Top Fuel/WRFPM, Orlando, Florida, USA, 2010, pp. 513–524*.
- [142] S. Abolhassani, G. Bart, J. Bertsch, M. Grosse, L. Hallstadius, A. Hermann, G. Kuri, G. Ledergerber, C. Lemaignan, M. Martin, S. Portier, C. Proff, R. Restani, S. Valance, S. Valizadeh, H. Wiese, *ASTM STP 1543* (2015) 540–573.
- [143] T. Seymour, P. Frankel, L. Balogh, T. Ungár, S.P. Thompson, D. Jädernäs, J. Romero, L. Hallstadius, M.R. Daymond, G. Ribárik, M. Preuss, *Acta Mater.* 126 (2017) 102–113.
- [144] G. Kuri, H. Ramanantoanina, J. Bertsch, M. Martin, I. Panas, *Corros. Sci.* 143 (2018) 200–211.
- [145] M. Chollet, S. Valance, S. Abolhassani, G. Stein, D. Grolimund, M. Martin, J. Bertsch, *J. Nucl. Mater.* 488 (2017) 181–190.
- [146] A.W. Colldewei, A. Baris, P. Spätig, S. Abolhassani, *Mater. Sci. Eng. A* 742 (2019) 842–850.
- [147] J. Hawes, A. Baris, Y.L. Chiu, S. Abolhassani, *J. Nucl. Mater.* 534 (2020) 152133.

- [148] G. Sundell, Atomic Scale Degradation of Zirconium Alloys for Nuclear Applications, Ph.D. Thesis, Chalmers University of Technology, 2015.
- [149] C. Dai, P. Saidi, Z. Yao, M.R. Daymond, *Acta Mater.* 140 (2017) 56–66.
- [150] C. Dai, F. Long, P. Saidi, L.K. Béland, Z. Yao, M.R. Daymond, *Phys. Rev. Mater.* 3 (2019) 043602.
- [151] G.J.C. Carpenter, D.O. Northwood, *J. Nucl. Mater.* 56 (1975) 260–266.
- [152] C. Jones, V. Tuli, Z. Shah, M. Gass, P.A. Burr, M. Preuss, K.L. Moore, *Sci. Rep.* 11 (2021) 4370.